

DC-side High Impedance Ground Fault Detection for Transformerless Single-phase PV Systems

A master thesis submitted by

Gang Wang

in partial fulfillment of the requirements for the degree of

Master of Science

in

Electrical Engineering

Tufts University

August 2016

Advisor: Professor Alex M. Stankovic

Abstract

With the fast development of the photovoltaic (PV) industry, techniques of improving solar cell efficiency, reliable and low cost inverter and advanced fault detection methods have been introduced. This thesis is focusing on ground fault detection on the DC side of a PV system.

Ground fault detection interrupter (GFDI) has been implemented in PV systems to detect ground faults and open the circuit during fault operations. However, GFDI is only effective for low impedance ground fault. For high impedance ground fault (HIGF), GFDI will not be triggered since there is not enough fault current flowing through the device. HIGF should be cleared in a PV system; otherwise, potential hazards will induce fire accident of the PV generation plant and it will result in electrical shock of system operator.

A common mode current detection method has been adopted in this thesis to distinguish normal operation and HIGF operation of PV systems. Common mode model of PV system is derived which combines stray capacitance of PV arrays and stray parameters of inverter and power transmission line. Normal operation and HIGF operation will display different characteristics at common mode resonant frequencies. PSIM simulation results validate the feasibility of our common mode current detection method.

Acknowledgements

My gratitude goes to my advisor, Prof. Alex M. Stankovic. He designed a good plan for my Master education and gave me helpful guidance in involving research problems. I strongly appreciate the support in academic research and concern for my daily life.

My gratitude also goes to my parents and grandfather. Thanks for the encouragement and unreserved love you gave me.

George Preble and Clifford Youn assisted me in getting familiar with the study environment and living surroundings at Tufts. Thanks for your help throughout the process.

Finally, I am grateful to Fraunhofer CSE USA for the grant that funded my Master research.

Contents

Abstract	ii
Acknowledgements	iii
List of Figures	vii
List of Tables	xi
CHAPTER 1: Introduction	1
1.1 Development of the photovoltaic industry.....	1
1.2 Advantages of utilizing solar energy	3
1.3 Issues that need to be addressed in PV systems.....	5
1.3.1 Ground fault protection.....	6
1.3.2 Arc fault protection	8
1.3.3 Line-to-line fault protection	11
1.4 Summary of thesis research outcomes	13
CHAPTER 2: PV Module Modeling and Simulation.....	14
2.1 Fundamental physical characteristics of solar cells	14
2.2 Mathematical modeling of solar cells	18
2.2.1 One diode model of solar cells.....	18
2.2.2 PSIM simulation of PV module	20
2.3 Electrical characteristics of solar cells	26
2.3.1 Maximum power point tracking algorithms (MPPT)	26
2.3.2 PSIM simulation of series and parallel connected PV modules with P&O algorithm.....	30
2.4 Common PV panels and its application	36
CHAPTER 3: Ground Fault Analysis in Single-Phase PV System.....	39
3.1 Introduction of common inverters in PV systems.....	39

3.1.1 Isolated PV grid connected systems	40
3.1.2 Non-isolated PV grid connected systems	42
3.2 Single-phase transformerless grid connected inverters in PV systems.....	44
3.2.1 Boost converter	45
3.2.2 Full bridge inverter and PWM switching techniques	46
3.2.3 Simulation results of PV systems	49
3.2.4 Simplified model of ground fault analysis.....	52
3.4 Detection problems with high impedance ground fault.....	55
CHAPTER 4: DC Side High Impedance Ground Fault Detection.....	57
4.1 Common mode model of single-phase full bridge inverter	57
4.1.1 Common mode description of transformerless single-phase PV system	57
4.1.2 Common mode model of transformerless single-phase PV system with stray components	59
4.2 Parameter estimation of PV systems.....	65
4.2.1 Common mode voltage source.....	65
4.2.2 Common mode stray parameters and grid current inductor.....	66
4.3 Resonant frequency analysis of common mode current	68
4.3.1 Simplified common mode model simulation.....	68
4.3.2 Common mode analysis of PV system with stray parameters	72
4.4 HIGF detection with resonant frequency spectrum	74
4.4.1 HIGF detection in simplified common mode model	74
4.4.2 HIGF common mode analysis of PV system with stray parameters ...	79
4.5 Conclusion of HIGF detection with CM current method	81
CHAPTER 5: Conclusion and Future Work.....	83

5.1 Conclusion	83
5.2 Future work.....	85
Bibliography	86

List of Figures

Figure 1.1 Roof installed PV system in German village	2
Figure 1.2 Global cumulative installed PV power from 2000 to 2013	3
Figure 1.3 Common ground faults of PV system	6
Figure 1.4 PV module high impedance ground fault.....	8
Figure 1.5 Negative rail ground fault (blind spot)	8
Figure 1.6 Series and parallel arc faults of PV module	9
Figure 1.7 Line-to-line faults in PV module	11
Figure 2.1 Energy band schematic.....	15
Figure 2.2 Schematic of photovoltaic effect theory	16
Figure 2.3 One diode equivalent circuit model of solar cell.....	18
Figure 2.4 Effect of series connection of solar cells	22
Figure 2.5 PV module math model in PSIM.....	23
Figure 2.6 Solar parameters at standard testing condition (STC).....	24
Figure 2.7 Ideal I-V and power curve of PV module output	25
Figure 2.8 I-V and power curve of PV module output based on PV module	25
Figure 2.9 P-D dynamic relationship curve	28
Figure 2.10 Divergence of P&O algorithm.....	29
Figure 2.11 PSIM simulation of single PV module with P&O algorithm	30
Figure 2.12 Magnitude of power and voltage at MPP of single PV module	31
Figure 2.13 PSIM simulation of series connected PV module with P&O algorithm	32

Figure 2.14 Magnitude of power and voltage at MPP of series connected PV modules	33
Figure 2.15 PSIM simulation of parallel connected PV module with P&O algorithm	34
Figure 2.16 Magnitude of power and voltage at MPP of parallel connected PV modules	34
Figure 2.17 Schematic of PV module connection of large scale generation system	35
Figure 3.1 Grid isolated PV inverter structure with power frequency operation..	40
Figure 3.2 Grid isolated PV inverter structure with high frequency operation	42
Figure 3.3 Non-isolated single-stage PV inverter	43
Figure 3.4 Non-isolated multi-stage PV inverter	44
Figure 3.5 Schematic of the single-phase transformerless grid connected inverter	45
Figure 3.6 Schematic of unipolar PWM switching pattern.....	47
Figure 3.7 Unipolar PWM switching mechanism with reduced switching losses	48
Figure 3.8 Schematic of PV array with Boost converter in PSIM.....	50
Figure 3.9 System rating at the output of boost converter	50
Figure 3.10 Schematic of single-phase grid connected full bridge inverter	51
Figure 3.11 Voltage and current at the inverter output	51
Figure 3.12 Simplified PV inverter model with DC source.....	52
Figure 3.13 Illustration of fault locations	53
Figure 3.14 Schematic of normal operation.....	53

Figure 3.15 Schematic of ground fault at positive power line (A)	54
Figure 3.16 Schematic of ground fault between PV arrays (B, C, D)	55
Figure 3.17 Schematic of ground fault at negative power line (E).....	55
Figure 4.1 Scheme of single-phase transformerless PV inverter.....	57
Figure 4.2 Scheme of single-phase transformerless PV inverter with stray components	59
Figure 4.3 Schematic of PV system model with separate voltage sources	61
Figure 4.4 Schematic of PV system model with common and differential voltage sources.....	62
Figure 4.5 Schematic of simplified PV system common mode model.....	63
Figure 4.6 Final common mode model of single-phase transformerless PV system	65
Figure 4.7 Common mode voltage scheme with unipolar PWM in full bridge inverter	66
Figure 4.8 Simplified model with constant CM voltage source	69
Figure 4.9 Common mode current at resonant frequency.....	70
Figure 4.10 Simplified model with unipolar PWM switching CM voltage source	71
Figure 4.11 Common mode current at resonant frequency.....	71
Figure 4.12 Full bridge inverter with stray parameters.....	72
Figure 4.13 Spectrum of common mode current with full bridge inverter	73
Figure 4.14 DC voltage source common model with HIGF	75

Figure 4.15 Common mode current spectrum with 400 ohms ground fault (DC source).....	76
Figure 4.16 CM voltage source model with HIGF	77
Figure 4.17 Common mode current spectrum with 400 ohms ground fault (CM voltage source)	78
Figure 4.18 HIGF operations of full bridge inverter with stray parameters	80

List of Tables

Table 2.1 Comparison between ideal and math equation simulation	26
Table 2.2 MPP simulation results summarization of different connection schemes	35
Table 2.3 Electrical specifications of common PV modules	37
Table 3.1 Configurations and outputs of grid connected PV arrays	49
Table 3.2 Illustration of ground fault current flows through GFDI.....	55
Table 3.3 Maximum impedance for indicating ground fault with Outback GFDI	56
Table 4.1 Common mode model parameters for PV system	68
Table 4.2 Resonant frequency information of different simulation models	73
Table 4.3 Resonant current at normal resonant frequency (20 kHz) with HIGF (DC source).....	76
Table 4.4 Resonant current at normal resonant frequency (20 kHz) with HIGF (CM voltage source)	78
Table 4.5 Resonant common mode current magnitude at 20 kHz (A)	80

CHAPTER 1: Introduction

1.1 Development of the photovoltaic industry

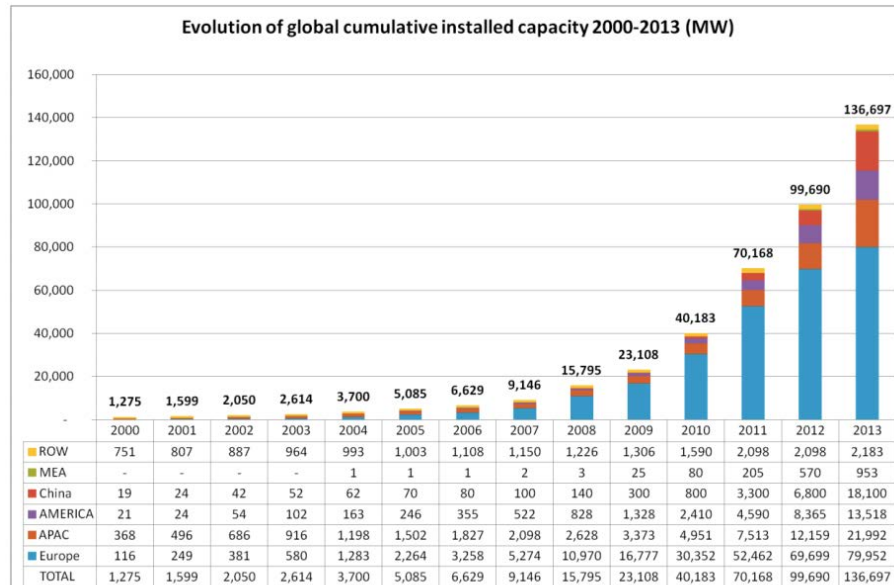
Photovoltaic technology utilizes natural sun irradiance to produce electrical energy. In 1954, Bell Lab discovered crystalline silicon based on PN junction, which was initially put into practical usage in spacecrafts. However, with the improved efficiency of solar cells, photovoltaic industry advanced in various areas, such as innovative materials for manufacturing solar panels, new topologies with high converting efficiency of PV inverter, and grid connected technics of electricity generation.

Improved efficiency of solar panels has contributed to the rapid growth of the PV industry in the past decades. For commercially applied solar cells, conversion efficiency ranges from 14 percent to 19 percent with the use of multicrystalline Si as the main building material [1]. Other, more exotic materials like gallium arsenide can build multi-junction concentrator solar cells with a maximum efficiency of 43.5 percent [2]. However, this high efficiency concept is difficult to apply in actual implementation of PV products due to the high cost to efficiency ratio compared with regular multicrystalline Si solar cells. In addition to the development of the advanced solar panels, intelligent and efficient algorithms for maximum power point tracking (MPPT) technology help to improve overall efficiency of the PV system. More details about MPPT algorithm will be presented in Chapter 2.



Figure 1.1 Roof installed PV system in German village

Germany was the first nation to mass-produce solar energy when German environmentalists obtained support from the government with 100,000 roof-installed PV systems in 2000. As of 2013, Germany's solar electricity production occupies the highest percentage of its national total electricity generation, 6 percent when compared with other countries. China, Japan and the United States are also investing a vast array of technical and human resources to develop the PV industry which will contribute to a significant growth of worldwide solar electricity capacity. Form the report of European Photovoltaic Industry Association (EPIA), the total amount of installed capacity increased 35 percent in 2013, reaching 136,697 MW, as shown in Fig. 1.2 [3][4]. With this rate of growth in solar electricity generation, EPIA estimates that PV energy will meet 10 to 15 percent of total European electricity consumption in 2030 and more than 20 percent of electricity will be provided by PV energy in 2050 [5].



Source: EPIA

Figure 1.2 Global cumulative installed PV power from 2000 to 2013

1.2 Advantages of utilizing solar energy

Past research [6] presented an estimate for calculating the amount of time remaining until fossil fuels will be depleted. It states depletion times for oil, gas and coal are 35, 37 and 107 years, respectively. Due to the limited remaining quantity and non-renewable characteristics of fossil fuels, an increasing number of countries are starting projects for developing the PV industry as it has unique advantages compared to other natural resources. Superior characteristics of solar energy are listed below:

- (1) Widely distributed and practically unlimited quantity

Most countries have enough sun irradiance for producing significant amount of solar energy. For those countries that have limited reserves of fossil fuels and

urgent requirements, solar energy becomes an important alternative. In addition, almost no country has the ability to monopolize solar irradiance. Accordingly, solar electricity generation market is a free and cost efficient area for almost every country in the world.

(2) High conversion efficiency from solar irradiance to electricity

Unlike wind, geothermal and hydraulic power generation, solar generation systems have no intermediate transformation involving thermal, mechanical and electromagnetic energy. Finally, a simplified electricity generating process can be achieved with solar cells. In addition, with improved technology of PV materials, general solar cells conversion efficiency can potentially reach from 30% to 50% in the next decade [8].

(3) Environmentally friendly and a low cost of productivity

The main material of solar cells is silicon, which is widely distributed on the Earth. Enhanced industrial techniques will likely further decrease the cost of producing solar cells. Thus, silicon-based solar cells can be sustainably produced in the future. Environmental problems are another significant issue brought up recently. During the operation of a PV system, there is no combustion process, which is different from fossil fuel energy generation; thus, emissions can be reduced.

(4) Easy maintenance and longtime usage

PV systems are easy to maintain in terms of daily service due to the rapid development in monitoring and control. Currently, each system typically contains equipment for automatic fault diagnosis, maximum power point tracking, sun irradiance tracking and functions. These methods guarantee safe operation and self-recovery of the PV system. In addition, most of photovoltaic panels can work for more than 30 years. In that case, the cost of long time operation and maintenance can be reduced significantly.

1.3 Issues that need to be addressed in PV systems

Advanced PV systems require less labor to maintain operation. Automatic control and detection algorithms or devices have been developed to help the system to work in a safe and efficient mode. In order to make PV systems operate normally, fault detection devices should always be embedded. Expected faults like ground fault, arc fault and line-to-line fault can be detected by GFDI, arc fault circuit interrupter (AFCI), and I-V curve based detection algorithms, respectively.

Constituent PV technologies are becoming mature and robust than the very beginning time of renewable energy development; problems like ground fault detection, arc fault detection, open faults, line-to-line faults and electromagnetic interference due to high switching frequencies have largely been resolved [9]. However, those methods can only solve basic problems in photovoltaic systems. The following passages will introduce several serious issues that need to be addressed in PV systems.

1.3.1 Ground fault protection

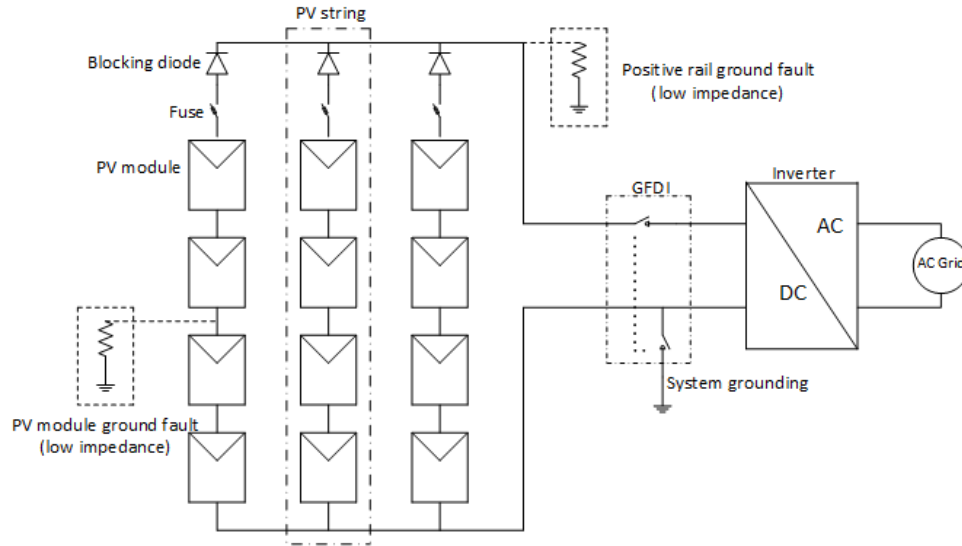


Figure 1.3 Common ground faults of PV system

Ground fault is a common fault in photovoltaic generation systems, which will induce electric shock to people and over-heating or even fires in PV panels. In addition, ground fault will lead to power losses and MPPT operation will be affected. Effective measures should be taken to prevent any kind of ground fault existing in PV systems.

From Fig. 1.3, we can see common ground fault occurring at the PV string and the positive rail. If there exists impedance connected between the PV array and ground, PV output current varies since part of current will flow through grounded impedance and create a path between the PV string, ground and the inverter. Normally, if the grounded impedance is relatively low, current will be large enough for triggering the GFDI device, which will protect the PV system from being damaged. However, not all the ground faults inside of PV panels show

characteristic of low impedance. There is a distinct possibility that ground impedance maybe high, or hides on the negative rail. In that case, we cannot see obvious power variation or overheating with hot spot techniques [10].

Low impedance ground fault in the positive rail or between the PV string can be easily detected due to variations of output power, as we can see from Fig. 1.4. In addition, we can also see voltage and current difference compared with normal operation of photovoltaic systems, which will trigger GFDI. However, as mentioned before, when high impedance exists on the positive rail, even a circuit path has created between PV array, grounded impedance and the ground fault detector, the GFDI device cannot detect it due to the limited current flows through this device. In Fig. 1.5, if the ground fault occurs at the negative rail, GFDI cannot sense enough current to disconnect the inverter due to the absence of a voltage source in the circuit path. In that case, effective detection methods and algorithms should be implemented in the PV system. However, currently there is no widely used effective method to detect high impedance fault. In this thesis, I will present useful detection measures of high impedance ground faults on the DC side of solar panels or blind spot on the negative rail. Both theoretical analysis and PSIM simulation prove that effective action can be taken with the newly proposed detection techniques.

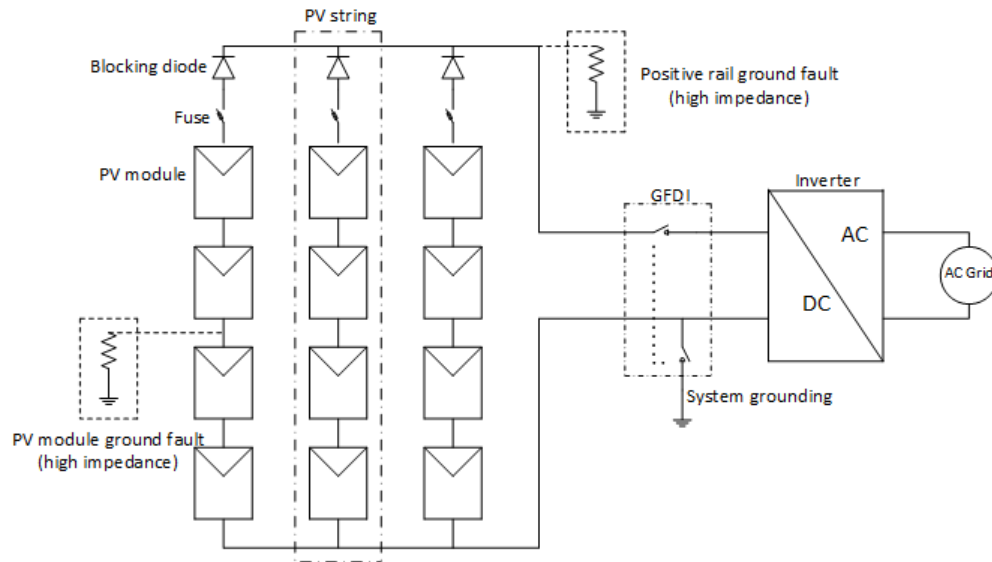


Figure 1.4 PV module high impedance ground fault

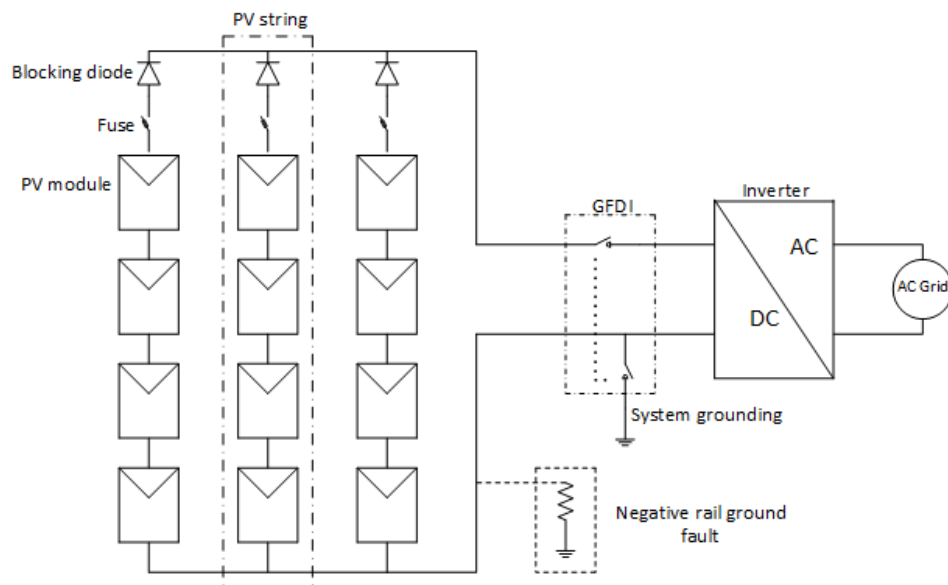


Figure 1.5 Negative rail ground fault (blind spot)

1.3.2 Arc fault protection

According to added section 690.11 of the national electrical code (NEC), it is mandatory to install AFCI to mitigate danger of rooftop fire or electrical shock for

users. As illustrated in Fig. 1.6, series arc-fault detection is currently required by NEC. However, parallel arc-faults like cross string line-to-line arc faults, intra string line-to-line faults and ground arcing faults are also common in photovoltaic systems. In addition, parallel arc-faults are more dangerous than series ones since a circuit can be formed even when the PV array is open. For a safe working system, each kind of arc-fault should be detected and removed by appropriate equipment.

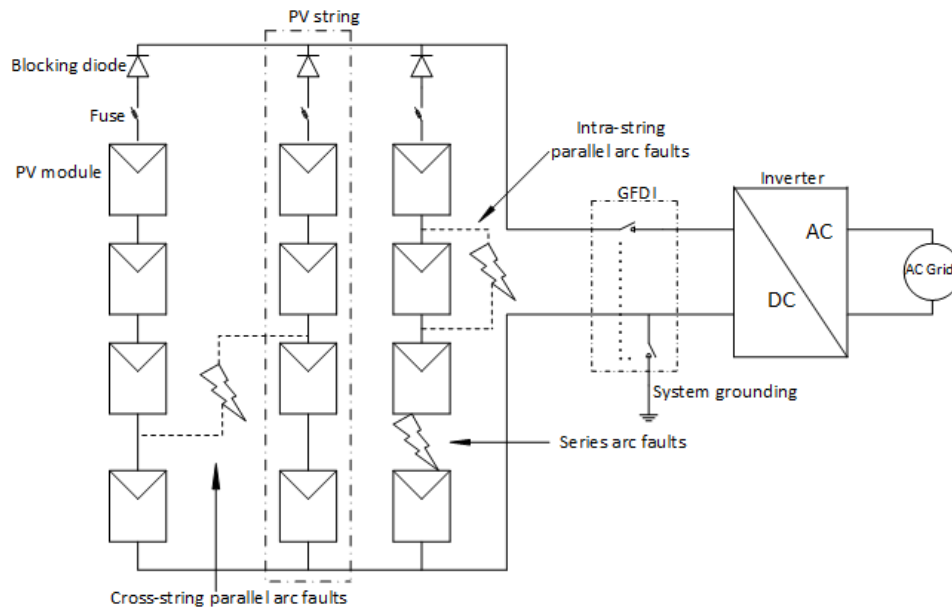


Figure 1.6 Series and parallel arc faults of PV module

Research presented in [11] simulates the electrical behavior of series and parallel arc-fault, which was conducted by Sandia National Laboratories. SPICE models were created to simulate series arc-faults in the string, intra-string parallel arc-faults, cross-string parallel arc-faults and arcing ground faults. Simulation results prove that for series arc-faults in the same location, maximum power

output is largely reduced with the increase of series arc resistance. However, series arc fault is independent of exact location of fault in the PV string. The parallel arc-fault is easy to distinguish from the series arc fault due to large variations of maximum power point voltage and open circuit voltage between the two fault types. However, it is hard to find exact locations of intra-string parallel arc-faults since the same arc impedance in a single string will result in the same I-V curve between different PV modules. For cross-string arc faults, different locations of connected PV module will have different I-V characteristics. Comprehensive simulation and testing will help understand exact location of cross-string arc faults. For ground arc-faults, the simulation result is similar to intra-string arc-faults except one terminal is connected to the ground. Precise location of arc terminal can be determined with careful calculation and simulation of every arc-fault location on each module.

A procedure for arc fault detection is described in [13]. Firstly, we need to prepare baseline measurements at different locations in the system, including the inverter and PV panels. With this information, we can get the system noise at each possible arc fault point of the PV system. For arc-faults, both time domain and frequency domain information were derived to analyze difference between normal operation and arc-fault operation. After understanding all the arc-fault characteristics, detection algorithms based on the time domain and frequency domain information can be derived.

A MCD estimator with current and voltage measurement and an AFCI with frequency domain analysis of PV array current are effective measures for series arc-faults [15][16][17][18]. Parallel arc-fault detection procedures are using a combination of current frequency domain analysis with a sudden drop of voltage and current magnitude with AFCI and sensing equipment [17]. A new method using spread spectrum time domain reflectometry (SSTDR) was applied in PV arc-fault detection in [12]. This method is not influenced by solar irradiance or DC voltage and current magnitude, which in turn can predict more accurate location and fault impedance. In addition, the SSTDR method can make a prediction before the operation of the PV system and remove the fault faster.

1.3.3 Line-to-line fault protection

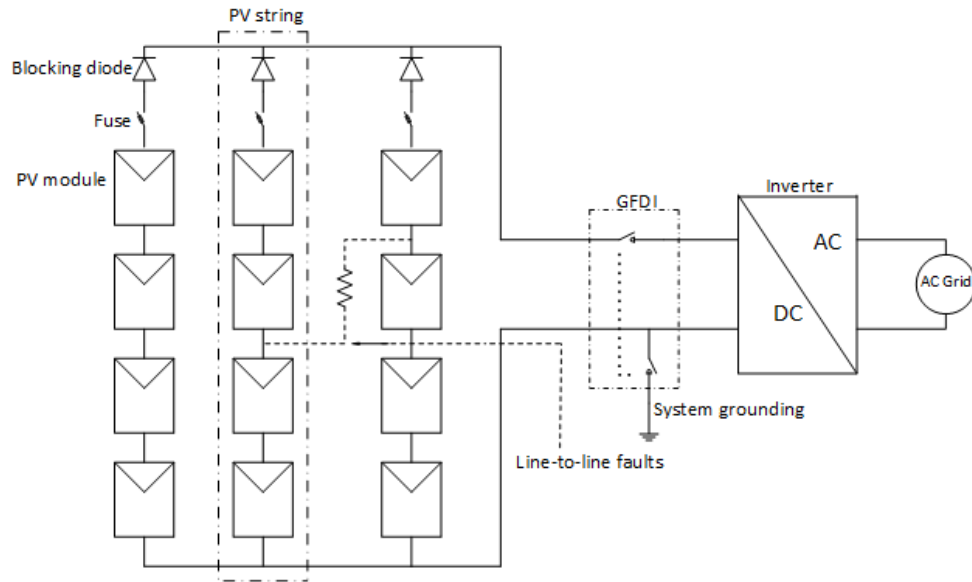


Figure 1.7 Line-to-line faults in PV module

Line-to-line fault is a common occurrence in PV modules. Similar to cross-string arc faults, line-to-line faults can be simulated and investigated by adding impedance between string modules. As we can see from Fig. 1.7, different location of connected PV modules can lead to large variations of output power. In addition, line-to-line faults also depend on sun irradiance and temperature [20]. Thus, in order to derive the relationship between line-to-line faults and output power, multiple cases should be studied for different connected impedances, weather conditions and module fault locations.

Several detection algorithms are presented in [19][21], where artificial neural network is adopted to diagnose line-to-line faults. It collects data like input current and voltage and other elements which will have an effect on the system behavior. After collecting data, a training process was conducted for getting significant information to validate accuracy of artificial neural network algorithms. A decision tree based algorithm was proposed to improve efficiency of real time detection and prediction accuracy.

Although numerous approaches have been published about detecting line-to-line faults, problems like high impedance fault between contended strings, low irradiance operation and low DC input voltage still need resolution.

Faulty conditions in PV systems are not limited to ground fault, arc fault and line-to-line fault. Hazards of switches open fault, bypass diode failure or cell degradation should also be taken into consideration during design stage.

1.4 Summary of thesis research outcomes

My thesis topic focused on DC side ground fault detection of single-phase transformerless PV systems. Chapters of this thesis are organized as follows: Chapter 2 establishes the basic model of PV modules and simulates the power variations of series and parallel connected PV modules. After understanding the effect of the number PV modules connected to output power, we attain a clear perspective of PV array open circuit, short circuit voltage and maximum power point features. Chapter 3 simulates the whole single-phase system with PV array, and full-bridge inverter. Different topologies of PV systems are discussed in this chapter. In addition, advantages and disadvantages of each topology and their applicable area are presented. This illustrates how a single-phase PV system is working and explains electrical characteristics of single-phase PV systems. Chapter 3 also simulates the ground fault with PV arrays, the MPPT algorithm and an inverter. The limitations of current ground fault detection method and the difficulty of high impedance ground fault are analyzed. Conclusions about the effects of ground faults to the operation of PV systems are reached and possible action of a fault protection device is examined through comparing industrial data sheets and simulation thresholds. In Chapter 4, a common mode circuit of single-phase PV systems is derived and simulations of common mode voltage and current under normal operation and ground fault operation are displayed. The result shows that common mode analysis of single-phase PV systems is an effective and robust detection method of ground fault, especially for high impedance faults.

CHAPTER 2: PV Module Modeling and Simulation

2.1 Fundamental physical characteristics of solar cells

Light is made up of photons and each photon contains energy to excite electrons to high level energy orbits. The energy of photons depends on the frequency, which is displayed as different colors of light. In 1905, Einstein explained an experiment that showed that ultraviolet light can provide enough energy for electrons to escape from the surface of a metal, which proves the photoelectrical effect of photons [22]. That experiment is the origin of solar cell electricity generation.

For a certain material, absorbing photons will transfer energy to electrons of material's atoms. Due to the variation of photon's carried energy, electrons of atoms can jump from low energy state to high energy state or even escape from atoms to become free moving. Quantum theory establishes that electrons of atoms can rotate at different orbits and electrons on each different orbit will have different energy. The electron on the low energy orbit can jump to high energy orbit with light or other energy absorbing mechanism. On the contrary, electrons that rotate in a high energy orbit will release energy when falling to low energy orbit.

Electrons rotate in energy orbits of crystals with more than one atom can evolve in the energy band. The area between two consecutive energy bands cannot be occupied by electrons and this area is called the forbidden band. Typically, electrons will occupy the lowest energy band first and occupy the closest higher energy band next. Bands with no electrons are called empty bands or conduction bands. Electrons located in the outer most energy band, or valence bands, are valence electrons. Energy bands higher than the valence band which are not fully occupied by electrons are called conduction bands. The energy difference between the top of valence E_v band and the bottom of the conduction band E_c is the forbidden band or bandgap, denoted as E_g . Fig. 2.1 illustrates the structure of energy bands. The phenomenon of electric conduction in a conductor or semiconductor is the effect of moving electric carried quantum. The carriers in a conductor are combined with free electrons, and negative electrons or positive holes in a semiconductor.

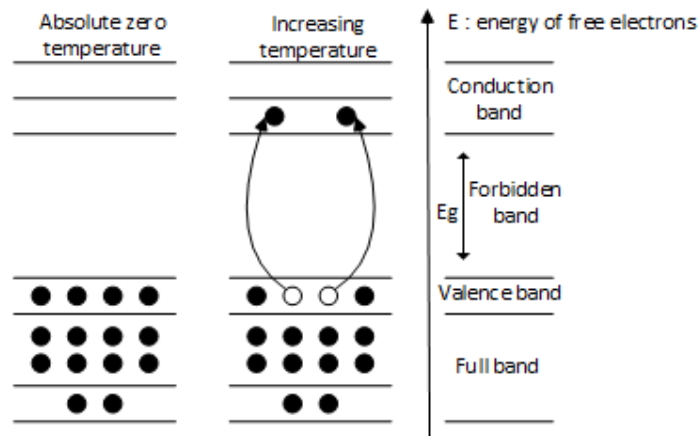


Figure 2.1 Energy band schematic

Semiconductors have excellent insulation properties near absolute zero temperature, and the number of carriers increases with temperature. All the valence electrons are circling in the valence band near absolute zero temperature. There is no electric conduction process since no electron exists in the conduction band. When the temperature increases, it will provide enough energy for electrons in the valence band to move to the conduction band. Actually, the electron is escaping the covalent bond of the semiconductor and a hole forms at the valence band consequently. Electron-hole-pairs (EHP) moving at certain directions create conductivity of semiconductor devices. Solar electricity generation is based on the semiconductor photovoltaic effect. This process can be described as an inherent change of charge distribution inside semiconductor material with sun irradiance. The following chapter introduces how photovoltaic effect generates current and voltage of solar panels.

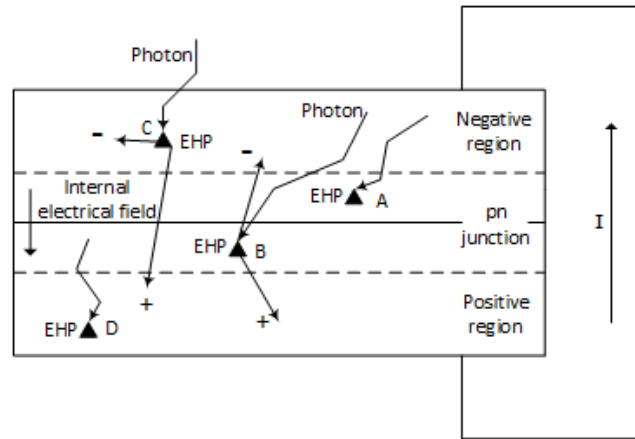


Figure 2.2 Schematic of photovoltaic effect theory

Absorbing photons will generate EHP; Fig. 2.2 illustrates how EHP will impact semiconductors. EHP A and B are generated inside PN junction. Under the

influence of an internal electrical field, the electron of EHP will move to the negative area, whereas hole of the EHP will move to the positive area. Consequently, main electrical parameters like electron density in the negative region and hole density in the positive region near the PN junction will increase. The increased carrier density will make carriers diffuse towards the outside contacts. Accordingly, a voltage is generated between top and bottom contacts. If the top and bottom of contacts are connected, current will be observed and it is proportional to the quantity of EHP. For ENP generated outside but very close to PN junction, like C and D in Fig. 2.2, a similar phenomenon will occur. The electron of D is a minor carrier in a positive region, and it can enter the PN junction area due to the thermal movement. This electron will enter negative region by the force of the internal electrical field, and become the major carrier in the negative region. Similarly, holes of C will eventually enter positive region, and turn to major carrier in positive region. As stated before, semiconductor devices will generate EHP due to light irradiance, and EHP will depart towards different destinations under the electrical field of PN junction. Accumulated electrons on the contact of negative region and holes on the contact of positive region will behave as voltage difference between the two contacts, and current will be detected if two contacts form an electrical circuit. This is the fundamental theory behind the use the photovoltaic effect in semiconductors to manufacture solar panels.

2.2 Mathematical modeling of solar cells

2.2.1 One diode model of solar cells

The PV module is composed of series and parallel connection of PV cells. For better understanding electrical features of the PV module, a PV cell model can be simulated and analyzed through the one diode equivalent circuit. Based on the physical characteristic of solar cells, the one diode equivalent circuit model is shown in Fig. 2.3. It takes all relevant parameters like temperature, irradiance level, and equivalent power loss resistance into consideration [23][24].

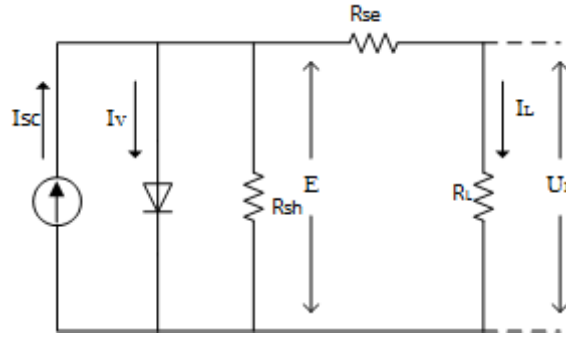


Figure 2.3 One diode equivalent circuit model of solar cell

I_{sc} represents the current, which is generated by photons in solar cells. It depends on the sun irradiance, body temperature and surface area of solar cells. I_{sc} is directly proportional to the sun irradiance and proportional to body temperature of solar cells. I_v is a total diffusion current of PN junction and it flows towards different direction against I_{sc} . R_{se} is a series resistor of solar cells. It consists of the body resistor, surface resistor, electrode conductor resistor and equivalent connection resistor between the electrode and surfaces of solar cells.

R_{sh} is a shunt leakage resistor of solar cells. It is caused by deficiency inside solar cell and impurities or humid surroundings of the silicon wafer.

Equations of load current can be expressed as:

$$I_L = I_{sc} - I_V - \frac{U_L + I_L R_{se}}{R_{sh}} \quad (\text{Eq. 2.1})$$

$$I_{sc} = [I_{scr} + C_i(T - T_r)] \left(\frac{S}{S_r} \right) \quad (\text{Eq. 2.2})$$

$$I_V = I_{D0} \left[e^{\frac{q(U_L + I_L R_{se})}{AKT}} - 1 \right] \quad (\text{Eq. 2.3})$$

$$I_{D0} = I_{D0r} \left(\frac{T}{T_r} \right)^3 e^{\left[\frac{qE_g}{AK} \left(\frac{1}{T_r} - \frac{1}{T} \right) \right]} \quad (\text{Eq. 2.4})$$

$$E_g = 1.17 - \frac{4.73 \times 10^{-4} * T^2}{636 + T} \quad (\text{Eq. 2.5})$$

I_L : Solar cell output current (A);

I_{sc} : Photon generated current or short circuit current (A);

I_V : Diode current (A);

U_L : Solar cell output voltage (V);

R_{se} : Series resistance (ohms);

R_{sh} : Shunt resistance (ohms);

I_{scr} : Reference short circuit at STC (A);

C_i : Temperature coefficient (A/K);

T : Actual ambient temperature (K);

T_r : Reference ambient temperature (K);

S : Actual solar irradiance (W/m^2);

S_r : Reference solar irradiance (W/m^2);

I_{D0} : Diode saturation current without irradiance (A);

q : Electron charge, 1.6×10^{-19} C;

K : Boltzmann constant, 1.38×10^{-23} J/K;

A : Diode ideal factor, $1 \leq A \leq 2$;

I_{D0r} : Reference diode saturation current (A);

E_g : Silicon based forbidden band energy (eV);

2.2.2 PSIM simulation of PV module

According to the one-diode model, a mathematical model can be created; with this math equation, we can establish a computational algorithm for the PV module in the PSIM environment. It is realizable in PSIM environment because we can add all relevant parameters, which will influence power characteristics of the solar cell. In addition, PSIM can integrate physical solar cell model with power electronic circuits, which displays clear advantages over Matlab/Simulink environment. Common parameters like the band energy, temperature coefficient

and diode saturation current can be directly obtained from tutorial of physical solar cell in PSIM [25].

The utility tool in PSIM provides a good method to estimate parameters of solar cells. There are three steps in deriving parameters of solar cells. Firstly, we need to enter the basic information from the datasheet provided by the solar cell manufacturer. Here we are going to use the solar module MSX-60 from BP solar. Information needed includes the number of series connected solar cells (N_s), maximum power output (P_{max}), voltage at maximum power point (V_p), current at maximum power point (I_p), open circuit voltage (V_{oc}), short circuit current (I_{sc}), light intensity and reference temperature (S_r). Secondly, initial guess of the band gap energy (E_g), ideality factor (A) and shunt resistance (R_{sh}) should be supplied. Finally, with the input information and initial guess data, model parameters like the series resistance (R_{es}), reference short current circuit (I_{scr}), reference diode saturation current (I_{D0r}) and temperature coefficient of short circuit current (C_i) are derived.

The PV module of MSX-60 is combined by 36 series connected solar cells. As we can see from Fig. 2.4, the equivalent series and shunt resistance is multiplied by 36. However, the short circuit current and diode saturation current are not influenced by series connection.

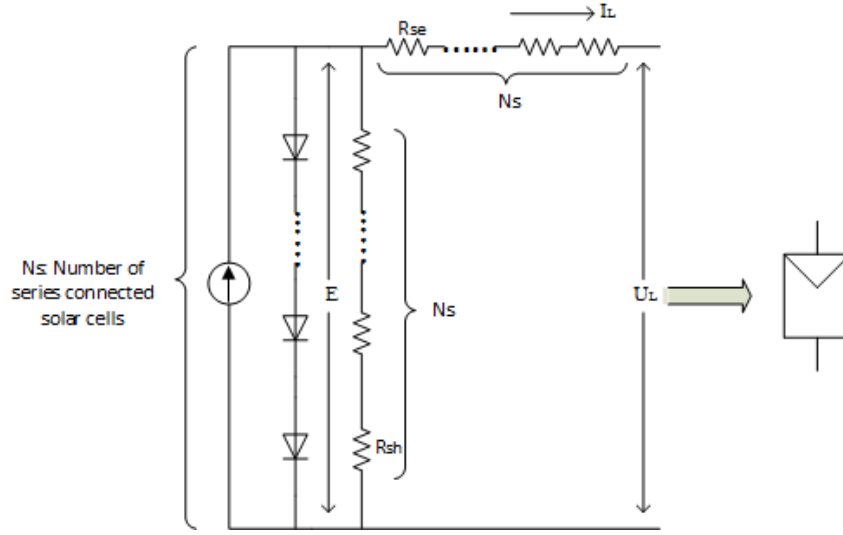


Figure 2.4 Effect of series connection of solar cells

Revised equations of series connected solar cells can be reached as follows:

$$I_L = I_{sc} - I_V - \frac{U_L + I_L * N_s * R_{se}}{R_{sh}} \quad (\text{Eq. 2.6})$$

$$I_{sc} = [I_{scr} + C_i(T - T_r)] \left(\frac{S}{S_r} \right) \quad (\text{Eq. 2.7})$$

$$I_V = I_{D0} \left[e^{\frac{q(U_L + I_L * N_s * R_{se})}{AKT}} - 1 \right] \quad (\text{Eq. 2.8})$$

$$I_{D0} = I_{D0r} \left(\frac{T}{T_r} \right)^3 e^{\left[\frac{qE_g}{AK} \left(\frac{1}{T_r} - \frac{1}{T} \right) \right]} \quad (\text{Eq. 2.9})$$

$$E_g = 1.17 - \frac{4.73 * 10^{-4} * T^2}{636 + T} \quad (\text{Eq. 2.10})$$

From the revised equation of solar cells, a PV module model based on the single diode method is established and simulated in PSIM below:

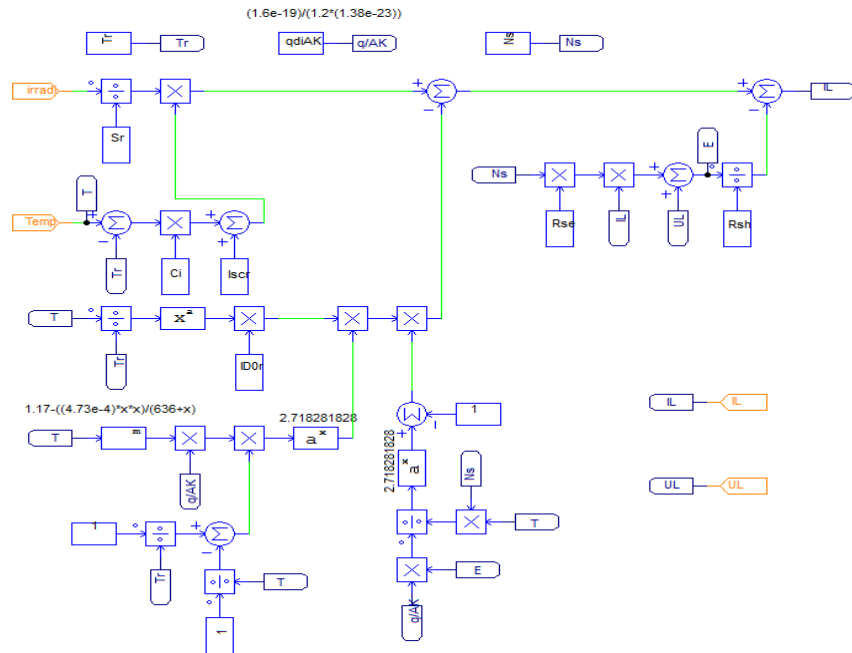


Figure 2.5 PV module math model in PSIM

Parameters from utility tool in PSIM are shown in Fig. 2.6.

Manufacturer Datasheet		
Number of Cells N_s :	36	
Maximum Power P_{max} :	60	(W)
Voltage at P_{max} :	17.1	(V)
Current at P_{max} :	3.5	(A)
Open-Circuit Voltage V_{oc} :	21.1	(V)
Short-Circuit Current I_{sc} :	3.8	(A)
Temperature Coeff. of V_{oc} :	-0.38	(%/oC or oK)
Temperature Coeff. of I_{sc} :	0.065	(%/oC or oK)
Standard Test Conditions:		
Light Intensity S_0 :	1000	W/(m*m)
Temperature T_{ref} :	25	(oC)
dv/di (slope) at V_{oc} :	-0.68	(V/A)
(if available)		
Model Parameters (defined)		
Band Energy E_g :	1.12	(eV)
Ideality Factor A :	1.2	
Shunt Resistance R_{sh} :	1000	(Ohm)
Coefficient K_s :	0	
Model Parameters (calculated)		
	Calculate Parameters	
Series Resistance R_s :	0.008	(Ohm)
Short Circuit Current I_{sc0} :	3.8	(A)
Saturation Current I_{s0} :	2.16e-8	(A)
Temperature Coefficient C_t :	0.0024	(A/K)
Operating Conditions		
Light Intensity S :	1000	W/(m*m)
Ambient Temperature T_a :	25	(oC)

Figure 2.6 Solar parameters at standard testing condition (STC)

Under this configuration of solar parameters, an ideal I-V and power output of the PV module are shown below:

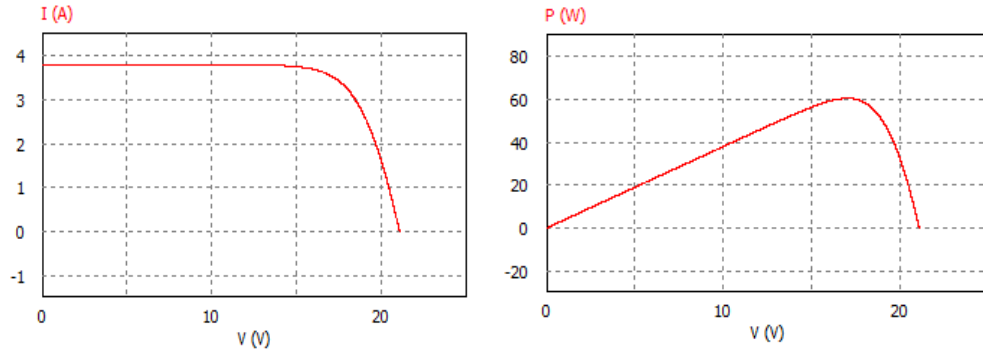


Figure 2.7 Ideal I-V and power curve of PV module output

For the given configuration of solar parameters, the power output derived by mathematical equations from one diode model is shown below:

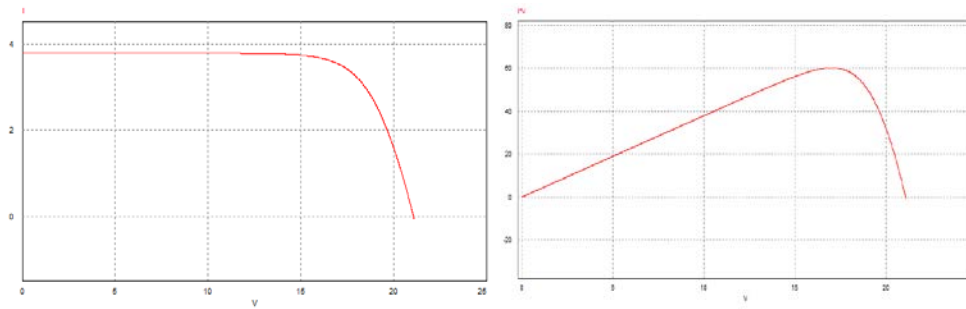


Figure 2.8 I-V and power curve of PV module output based on PV module

From the ideal and mathematical equation based on the I-V and power output of PV module, Table 2.1 was created to compare the difference between the ideal case and mathematical equation based case, and validates the effectiveness of the mathematical equation model of PV module.

From Table 2.1, the short circuit current, open circuit voltage, maximum power point of ideal outputs provided by PSIM utility tools and simulation outputs based on the one diode mathematical equation of the PV module are in

good agreement. Simulation results demonstrate that it is effective to use the one diode model to represent the current and voltage relationship of solar cells.

Simulation method	$I_{sc}(A)$	$V_{oc}(V)$	$I_p(A)$	$V_p(V)$	$P_{max}(W)$
Ideal outputs	3.80	21.10	3.55	17.04	60.53
Mathematical equation simulation outputs	3.80	21.08	3.54	17.02	60.25

Table 2.1 Comparison between ideal and math equation simulation

2.3 Electrical characteristics of solar cells

In the last section, we applied the one diode model to derive a relationship between the PV module current and voltage. From the output map of a PV module, we can clearly see that the solar module has special characteristics, different from ideal voltage and current sources. Each solar cell should work at maximum power point to achieve better power performance. In the section, I will introduce several common algorithms applied to the industrial PV inverter, and simulate the perturb-and-observe algorithm in PSIM environment. After testing electrical characteristics of the single PV module, series and parallel connection of PV modules needs to be evaluated to achieve large scale power performance.

2.3.1 Maximum power point tracking algorithms (MPPT)

MPPT algorithms need to be implemented in order to reach the maximize efficiency of PV modules. Commonly adopted approaches, such as the fractional open-circuit voltage and short-circuit current, hill climbing, perturb and observe

(P&O) and incremental conductance methods are applied in industrial power generation systems. All of these measures have their advantages, but also significant drawbacks. Next, we outline each method:

(1) Fractional open-circuit voltage and short-circuit current method

Fractional open-circuit voltage and short-circuit current approach is the one of the most convenient and easily implemented method [27]. Firstly, we measure the open circuit voltage of PV array. According to the estimated value of voltage at maximum power point, one can derive an equation for V_p .

$$V_p = k_1 * V_{OC} \quad (\text{Eq. 2.11})$$

V_{OC} is the open-circuit voltage and k_1 is the estimated coefficient of MPP. After testing numerous PV array outputs, it was concluded that k_1 usually varies from 0.71 to 0.78. Similarly, the maximum current point is equal to the coefficient k_2 times I_{sc} , which will give us I_p . The power point determined here cannot be fully guaranteed to equal the maximum power point. In addition, open circuit and short circuit are needed for testing power output, which will give a further decrease in total power production. Although this method is easy to understand, the desirable characteristics of good dynamics, low oscillations around MPP, and maximum power point cannot be reached. Accordingly, this measure is not widely used by industry.

(2) Hill climbing method

Hill climbing method forces $\Delta P/\Delta D$ to zero at MPP [28], where P represents the power output of the PV array and D stands for the duty ratio of the converter. In Fig 2.9, at the left side of MPP, duty ratio will increase to improve the output voltage while decrease it at the right side of MPP. However, hill climbing can be easily deceived under rapidly changing environments. For example, when the PV array undergoes a sudden increase or decrease of sun irradiance, the controller may be confused with the direction of operating point. This process can be resolved by slowing down the speed of hill climbing.

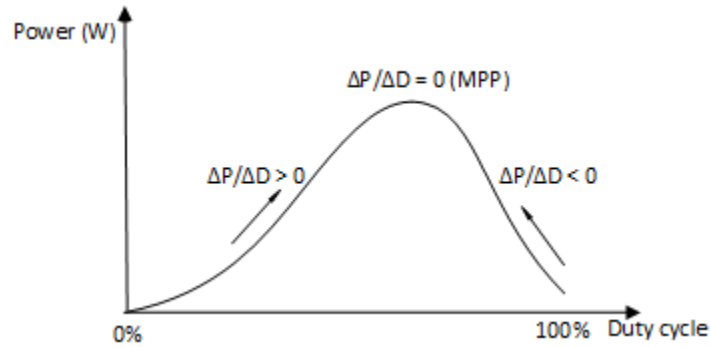


Figure 2.9 P-D dynamic relationship curve

(3) Perturb and observe method (P&O)

Perturb-and-observe method is quite similar to hill climbing since the system is just applying perturbation on the operating voltage [29]. A drawback of P&O MPPT technique is that operating point oscillates around MPP, which may cause the waste of energy. Also, the P&O algorithm can break down under quickly changing atmospheric conditions. The operating point will deviate from the MPP instead of approaching it. However, perturb and observe method is relevant when

considering benefits of MPPT algorithm and accuracy of maximum power point. In Fig. 2.10, A is the start point, and increase the perturb voltage which will automatic result in a power drop in B. However, if the solar irradiance changed significantly during one perturbation cycle, which gives us P_2 curve, and the total power is increased in point C compared with point A. Thus, P&O algorithm will give further voltage increase that can lead to the power drop in P_2 . Thus, P&O algorithm has failed in this situation. However, due to the fast response of P&O algorithm, power losses during environment changing cases are limited.

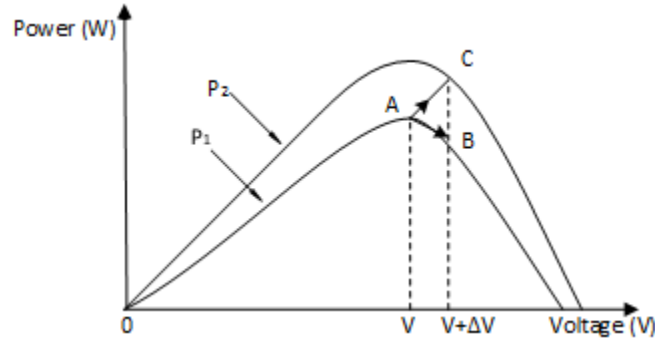


Figure 2.10 Divergence of P&O algorithm

(4) Incremental conductance algorithm (INC)

The process to achieve INC maximum power point tracking can be described as follows [30]: the output voltage is increased at the left side of MPP and automatically tuned at the right side. The theory of method is:

$$\frac{\Delta P}{\Delta V} = \frac{\Delta(V \cdot I)}{\Delta V} = \frac{(\Delta V \cdot I)}{\Delta V} + \frac{(\Delta I \cdot V)}{\Delta V} = V \cdot \left(\frac{I}{V} + \frac{\Delta I}{\Delta V} \right) \quad (\text{Eq. 2.12})$$

If $\Delta P/\Delta V$ is greater than zero, which means $I/V > -\Delta I/\Delta V$, the output voltage increases through step changes and decreases if $\Delta P/\Delta V$ is below 0. The step change is the variation of duty ratio. This algorithm can have the maximum power point when $\Delta P/\Delta V$ is exactly equal to zero.

2.3.2 PSIM simulation of series and parallel connected PV modules with P&O algorithm

By using the embedded P&O computation algorithm in PSIM environment, a single PV module, series connected PV modules and large scale connected PV modules are simulated and compared in the section, respectively. The model MSX-60 from SOLAREX is adopted in this environment as the basic PV module.

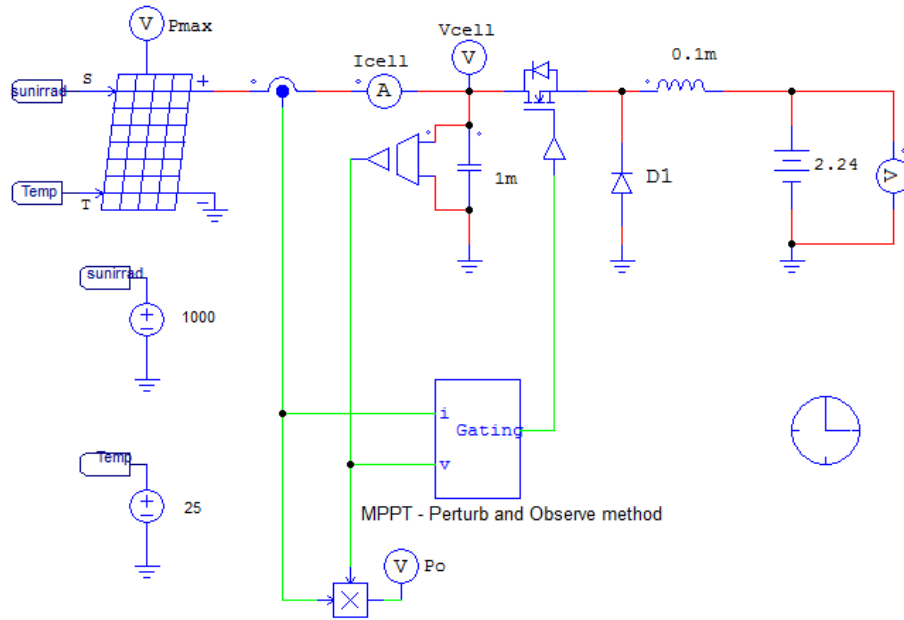


Figure 2.11 PSIM simulation of single PV module with P&O algorithm

Fig. 2.11 shows the schematic of single PV module, which is embedded with perturb and observe algorithm. From magnitudes of I_{cell} and V_{cell} , we can calculate the maximum power output of single PV module. By comparing simulation results with ideal parameters from SOLAREX, the effectiveness of MPPT algorithm and circuit schematic can be validated.

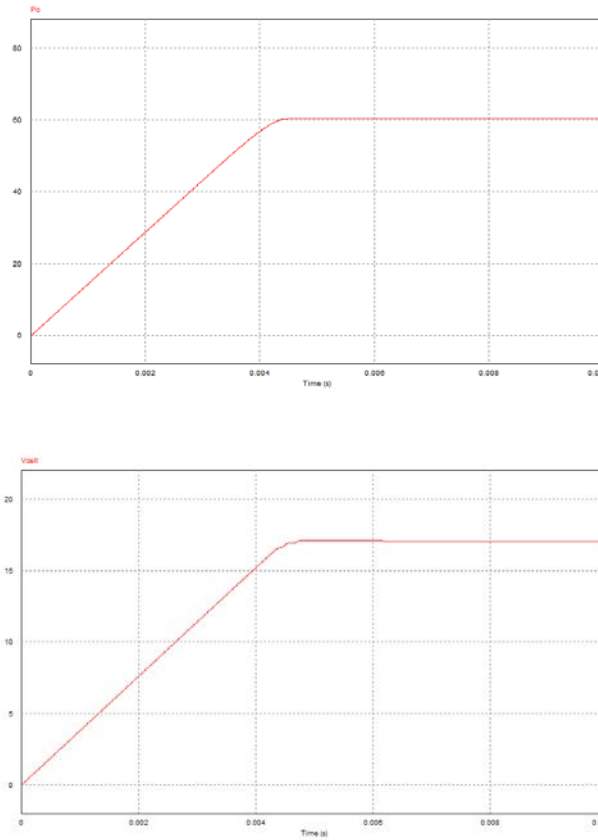


Figure 2.12 Magnitude of power and voltage at MPP of single PV module

Magnitudes of power, voltage and current at MPP can be read from simulation results of the single PV module, which are 60.53W, 17.08V and 3.54A respectively. Ideal parameters from SOLAREX datasheet are 60.49W, 17.04V and 3.55A respectively. Power losses of simulation results are within the

limitation range, which is 0.07% of ideal power output. In addition, the response time of reaching MPP is 4.30ms, and energy loss during this period is negligible.

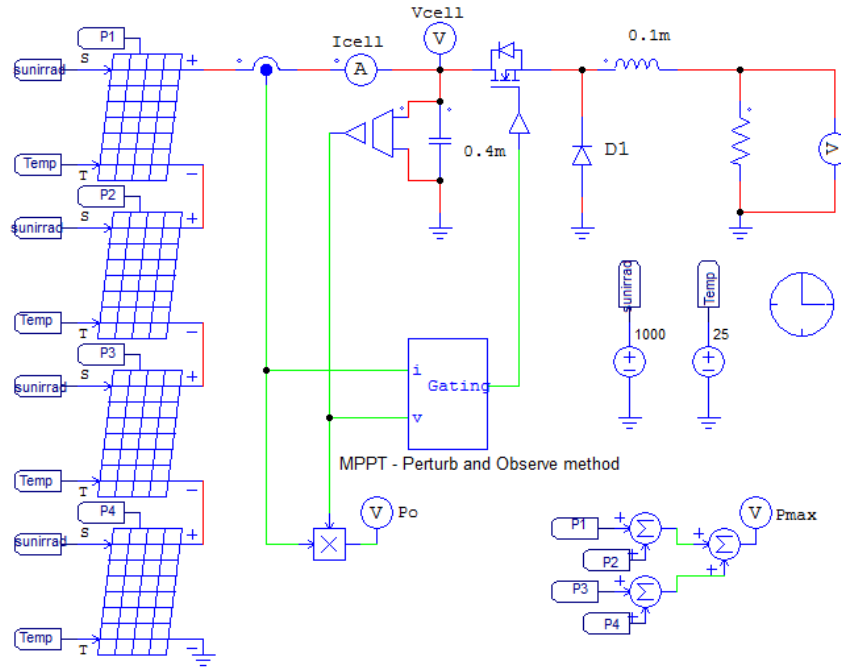


Figure 2.13 PSIM simulation of series connected PV module with P&O algorithm

Fig. 2.13 and Fig. 2.14 display diagrams, and voltage and power outputs of series connected PV modules. The voltage, current and power at maximum power point is 72.50V, 3.78A and 273.71W, respectively. Since series connected PV modules are combined from 4 single PV modules, the output current should maintain the same magnitude as the single PV module, while power and voltage should increase to 4 times of the single PV module output. The ideal single PV module outputs are 17.04V, 3.55A and 60.53W. However, for series connected PV modules, magnitudes of power and voltage at maximum power point are 4

times higher than single PV module outputs due to the power storage in the capacitor near solar panels.

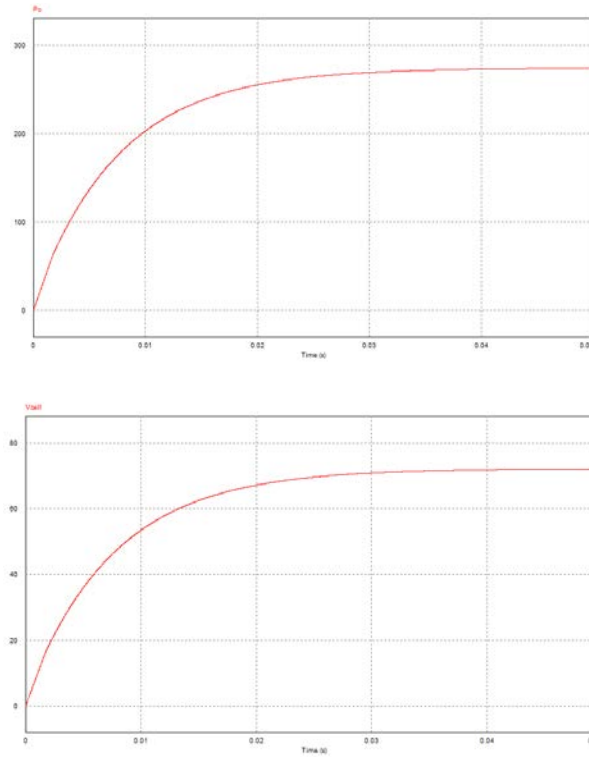


Figure 2.14 Magnitude of power and voltage at MPP of series connected PV modules

Fig. 2.15 and 2.16 show the schematic, and voltage and power outputs of parallel connected PV modules. This schematic is expected to have three times of the power and current magnitudes than series connected PV modules in Fig 2.13. From simulation results, we can find the voltage, current and power outputs of parallel connected PV modules are 72.80V, 11.39A and 829.19W, respectively. Power and current magnitudes of parallel connection scheme are almost three times of single string simulation, which are 3.78A and 273.71W in the series

connection schematic. Table 2.2 summarizes simulation results of the single PV module, series connected PV modules and parallel connected PV modules.

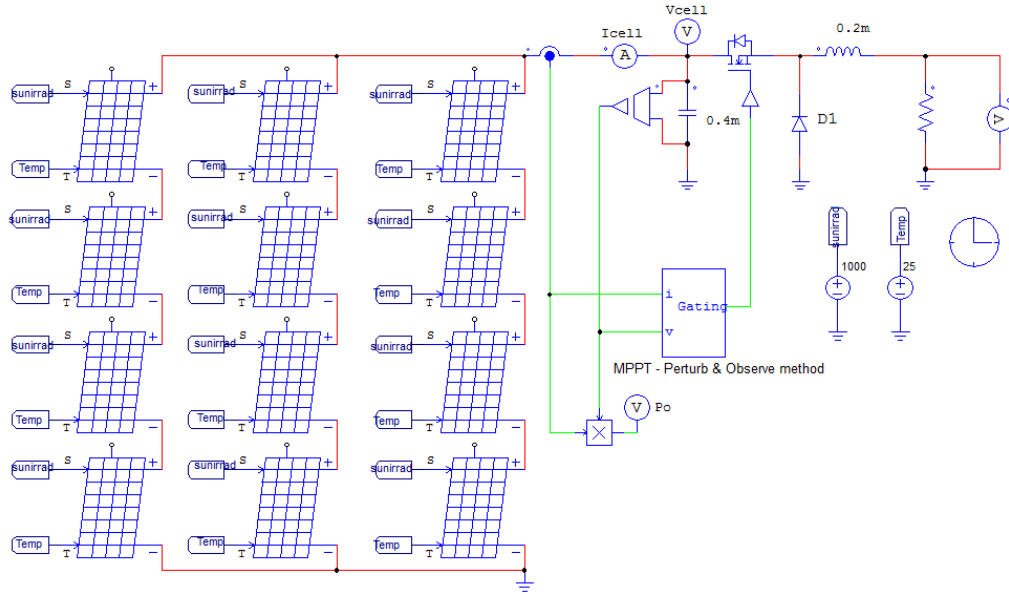


Figure 2.15 PSIM simulation of parallel connected PV module with P&O algorithm

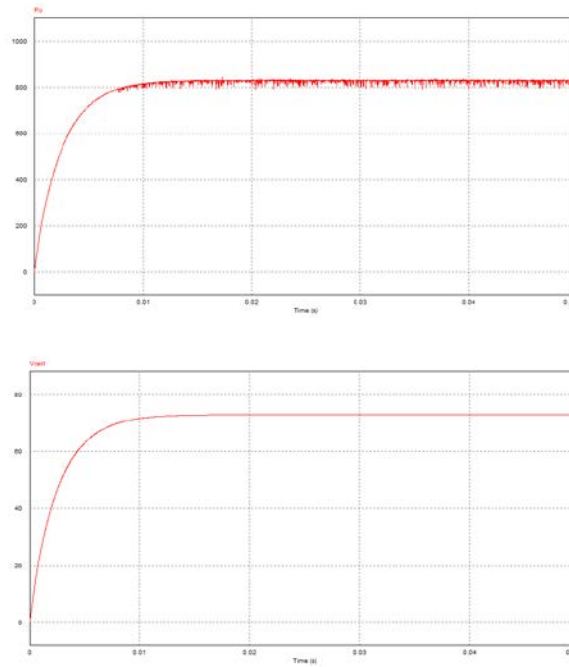


Figure 2.16 Magnitude of power and voltage at MPP of parallel connected PV modules

Type of PV module connection	$I_p(\text{A})$	$V_p(\text{V})$	$P_{max}(\text{W})$
Single PV module (1×1)	3.54	17.08	60.53
Series PV connection (4×1)	3.78	72.50	273.71
Parallel PV connection (4×3)	11.39	72.80	829.19

Table 2.2 MPP simulation results summarization of different connection schemes

Through evaluating magnitudes of current, voltage and power of the single PV module, series connected PV modules and parallel connected PV modules, equation 2.13 can be derived to describe the relationship between power and number of PV modules.

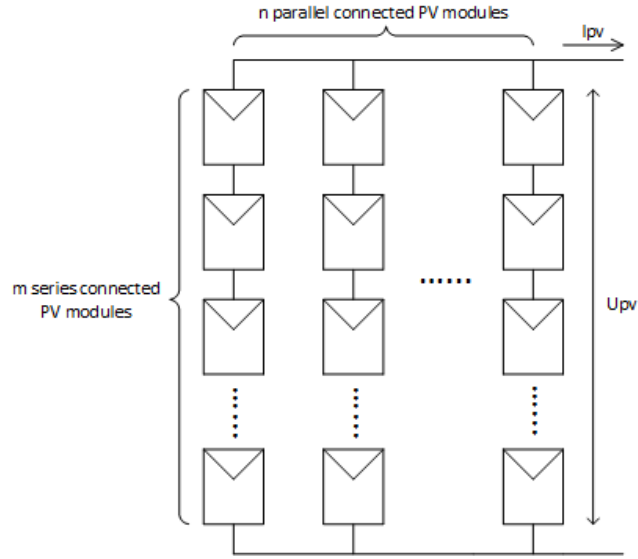


Figure 2.17 Schematic of PV module connection of large scale generation system

$$P_{total} = m \times n \times P_{single} \quad (\text{Eq. 2.13})$$

P_{single} is the maximum output power of single PV module;

P_{total} is the maximum output power of whole PV generation system;

m is number of PV module series connected in a single string;

n is number of PV string parallel connected in a whole PV generation system;

2.4 Common PV panels and its application

Many factors need to be considered when selecting solar panels. The cost of solar panels, power ratings, converting efficiency, maintenance costs and safety protections are most important issues in solar panels. Solar generation power plants tend to choose the high power rating, durable and low cost PV panels in order to achieve maximum commercial benefits. However, high safety protection standards, and easy maintenance procedures are key points for home used solar panels. In this section, several commonly used solar panels and their electrical characteristics are described. Table 2.3 shows electrical parameters of each PV module.

(1) Solarex MSX-60 [26]

This PV module was adopted in PSIM simulation environment. The most obvious advantage of this module is cost, making it virtually every industrial area. MSX-60 is covered by industry leading limited warranty, which guarantees the minimum P_{max} output when they purchased and more than 80% of minimum P_{max} for twenty years. The quality of these modules is certified from ISO 9001 to

higher standard requirements and complies with specifications of IEC 125, IEEE 1262 and CEC 503.

Module type	I_{sc} (A)	V_{oc} (V)	I_p (A)	V_p (V)	P_{max} (W)
Solarex MSX-60	3.8	21.1	3.5	17.1	60
Kyocera KD315GX-LPB	8.50	49.2	7.92	39.8	315
Canadian Solar CS6X-300M	8.74	45.0	8.22	36.5	300
Grape Solar GS-S-390-TS	8.42	59.6	7.92	49.4	341

Table 2.3 Electrical specifications of common PV modules

(2) Kyocera KD315GX-LPB [31]

KD315GX-LPB module is almost a maintenance free and reliable DC power source, which is designed to operate at highest level of efficiency among commercial PV modules. The normal rainfall is enough for cleaning module glass surface, and annual check is needed to prevent loose connections of wiring. Based on the high efficiency, less maintenance and safety protection characteristics, this module is a good choice for home use.

(3) Canadian Solar CS6X [32]

Key features of this module include the high converting efficiency up to 16.16%, self-cleaning surface and outstanding performance at low irradiance. Warranties of this module include 25 years coverage. From the certificates point of view, CS6X type module is compatible with IOS 9001, ISO/TS16949,

ISO14001, QC080000 HSPM, OHSAS 18001 and most of IEC standards. However, the cost of this module is higher than other commercial products because of the long time warranty and robust operation. Therefore, this module is a good option for applicatory which require high power quality.

(4) Grape Solar GS-S-390-TS [33]

This model has efficiency up to 18% with the long term stability and reliability. Holding the certifications of UL-1703, ISO 9000, CE, TUV, IEC61215, IEC61730, long time warranty is promised. In addition, it has outstanding performance during the high environment temperature and low irradiance condition. This module is suitable for small scale grid connected solar power stations, and commercial or residential roof-top PV systems.

CHAPTER 3: Ground Fault Analysis in Single-Phase PV System

As discussed in Chapter 1, there are many kinds of faults which can occur in PV system. Ground fault is one of the most common faults, and it will cause electrical hazard or even threaten human life. In this chapter, I will first introduce common inverters in a PV system, and describe how inverter works in PV systems. Then, single-phase transformerless grid connected PV inverters are simulated to analyze their electrical characteristics. With the topology of a single-phase PV system, different locations of ground faults are tested and their influences on the output are evaluated. Finally, a PV system with high impedance ground fault on the DC side is investigated, which is hard to detect with normal indication measures.

3.1 Introduction of common inverters in PV systems

An inverter is a significant part of solar generation system. It provides functions of MPPT tracking, DC/AC transformation, signal filtering and control algorithm optimization. Inverters not only influence the stability, safety, reliability and efficiency of grid connected distributed system, but also play an important role in evaluating performance of the whole system. Accordingly, a practical, reliable and low-cost inverter should be designed to support operation of the PV system.

We can classify PV inverters into two main types: one is electrical isolated from grid and another is electrically non-isolated from grid. Different types of inverters are selected for different uses in order to maximize inverter performance.

3.1.1 Isolated PV grid connected systems

PV systems with transformer isolation can protect users from electric shock when people occasionally touch the positive or negative rail of the DC side. It improves safety standards of the PV system. In addition, DC components will be blocked by the transformer, which keeps the distribution transformer from being saturated. There are two working modes of isolated transformer. One is working as power frequency and another is working at frequency 10 kHz or higher.

(1) Inverter with power switching frequency

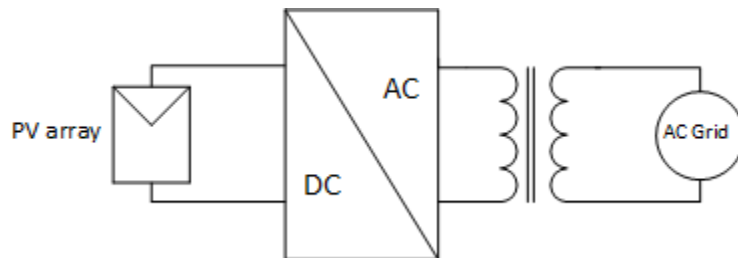


Figure 3.1 Grid isolated PV inverter structure with power frequency operation

DC voltage generated by PV panels is transferred to AC with an inverter at power frequency (60 Hz in U.S.) and connected to the grid after boosting voltage magnitude and isolating through the transformer. A simple diagram of this inverter type is shown in Fig 3.1. The advantages of the system are simple structure, high reliability, good safety operation and no injected DC component.

However, the disadvantages are heavy, large size, noisy and have low converting efficiency due to power frequency operation of transformer.

(2) Inverter with high switching frequency

To address the large size and heavy weight issues of the power frequency transformer, a high switching frequency operation inverter can be designed. Thus, the system can adopt a high switching transformer which will decrease the size and weight of the inverter. More power processing stages need to be inserted in order to convert high switching signal into power frequency. Accordingly, power losses will be increased in the system. However, with improved techniques of control strategy and power semiconductors, system efficiency has increased significantly with this topology. Schematic of two types of isolated high switching frequency PV inverter is shown in Fig 3.2.

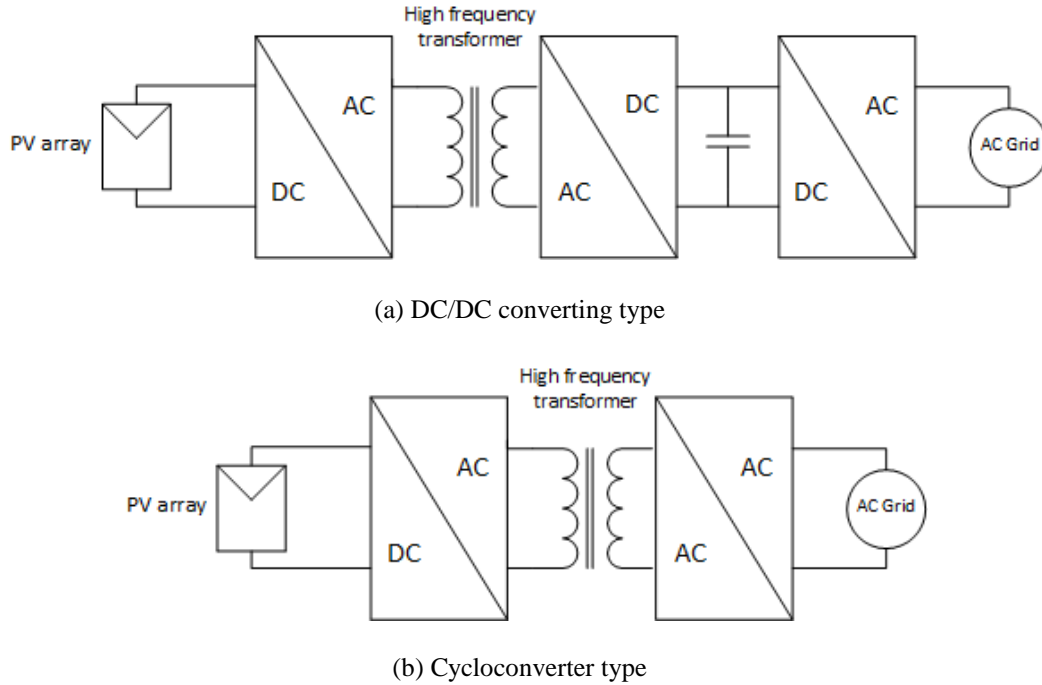


Figure 3.2 Grid isolated PV inverter structure with high frequency operation

3.1.2 Non-isolated PV grid connected systems

During the operation of the isolated PV grid connected system, electrical energy from PV panels is converted to magnetic energy, and transformed back to electrical energy. This process clearly causes energy losses. For a low power transformer, losses can reach up to 5% for energy conversion. In that case, the most efficient measure is designing non-isolated PV grid connected inverter. In this topology, we do not need to implement heavy and large power frequency transformer. In addition, complex-converting stages of high frequency transformer can be removed, which will simplify the design process and further reduce the cost of PV systems.

Non-isolated PV grid connected systems can be classified into single-stage energy conversion and multiple-stage energy conversion structures.

(1) Single-stage PV structure

For single-stage non-isolated PV inverter, solar arrays are connected to the grid directly through inverter in Fig 3.3. This system requires high DC voltage of solar arrays, which imposes higher electricity insulation standards on PV system in order prevent users from being shocked. This system is not applicable in actual electricity generation since we cannot guarantee high and stable DC voltage input of solar arrays. The output voltage and current of solar arrays are determined by irradiance, and temperature changes of ambient environment. In addition, maximum power point cannot be tracked with this topology. The existence of a single stage will contribute high conversion efficiency of the inverter; however, we will lose more if maximum power point is not reached. Thus, inverters with MPPT topology and DC/AC transformation are designed to achieve better performance of PV system.

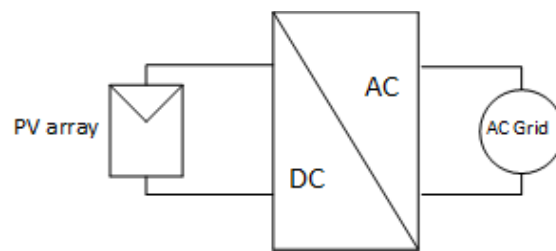


Figure 3.3 Non-isolated single-stage PV inverter

(2) Multi-stage PV structure

Compared with the single-stage non-isolated PV inverter, a multi-stage PV inverter has at least two energy processing steps. In Fig 3.4, power conversion stages are series connected by DC/DC and DC/AC topologies. As we discussed earlier, output power of solar arrays is determined by sun irradiance and temperature. In that case, output voltage of solar arrays is not always matching grid voltage rating and we need additional topology to adjust solar array output voltage before feeding grid. Thus, DC/DC topology is applied to track maximum power point of PV array and adjust output voltage. We can also label the multi-stage non-isolated PV inverter as high frequency non-isolated PV inverter since the modulation frequency of DC/DC converter is around thousand times higher than power frequency. Considering high efficiency, low weight, low cost and small size of this converter, this topology is widely used and likely to be improved in future applications.

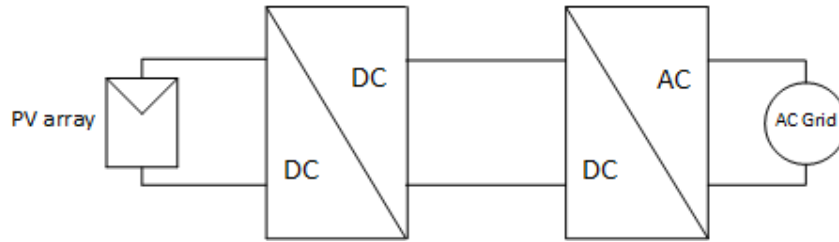


Figure 3.4 Non-isolated multi-stage PV inverter

3.2 Single-phase transformerless grid connected inverters in PV systems

In order to analyze normal operation and ground fault operation of PV systems, a single-phase multi-stage transformerless grid connected inverter was built in PSIM environment. As shown in Fig 3.5, it consists of PV array, boost

converter and full bridge inverter. I will analyze each function block of this system with simulation results and propose a simplified model to evaluate ground fault operation.

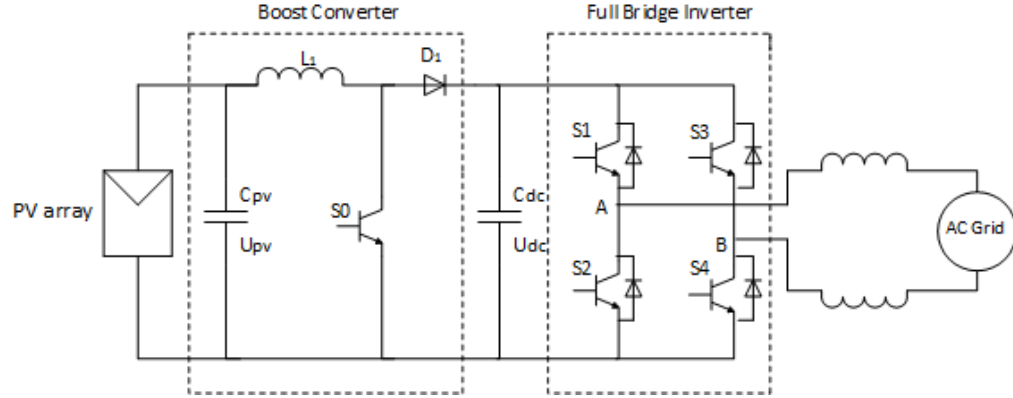


Figure 3.5 Schematic of the single-phase transformerless grid connected inverter

3.2.1 Boost converter

Under certain sun irradiance and temperature conditions, the PV array needs MPPT algorithm to achieve its optimal operating point. In addition, the voltage output of PV array is unlikely to meet the requirement of grid rating during low irradiance. Accordingly, a boost inverter is adopted here to find the maximum power point of PV array and increase output voltage before feeding power to the grid. The working procedure of boost converter is analyzed below:

T_S is the switching cycle of S_0 and D is the duty ratio in each period.

$0 < t < DT_S$: Switch S_0 is on during this period. The direction of PV current is $C_{pv} \rightarrow L_1 \rightarrow S_0$ and PV current goes back to negative terminal of C_{pv} finally. L_1 was charged among this duty ratio and $U_{pv} = U_{L1}$.

$DT_S < t < T_S$: Switch S0 is off during this period. The direction of PV current is $C_{pv} \rightarrow L_1 \rightarrow D_1 \rightarrow C_{dc}$ and it flows back to C_{pv} at the end.

Assuming L_1 works in continuous mode, current equilibrium equation of L_1 can be derived in one cycle:

$$U_{dc} = \frac{1}{1-D} U_{pv} \quad (\text{Eq. 3.1})$$

The output voltage of boost converter is higher than input voltage of solar arrays. With this configuration, solar arrays can connect to the grid regardless of the magnitude of the voltage output. In addition, maximum power point can be found with perturb and observe algorithm through measuring current and voltage at the input of boost converter.

3.2.2 Full bridge inverter and PWM switching techniques

Full bridge topology is widely used in single-phase PV inverters especially in high voltage applications. The output terminal DC voltage of full bridge inverter is U_{pv} , which is double in magnitude compared with the half bridge inverter. However, the voltage across transistor maintains the same level when the switch is turning off. In addition, half bridge inverter requires two split capacitors at DC side, which will increase the cost of inverter. So, full bridge inverter can have higher output voltage performance and cost-efficient characteristic than half bridge inverter.

Four switches of the full bridge inverter are modulated by pulse width modulation (PWM) signals. Common used PWM switching methods include

unipolar and bipolar switching [35]. High current ripples will be injected into grid by utilizing bipolar PWM method and switching losses of bipolar PWM is approximately twice than unipolar PWM. Finally, unipolar PWM switching is adopted here. The schematic of unipolar PWM switching is displayed in Fig 3.6.

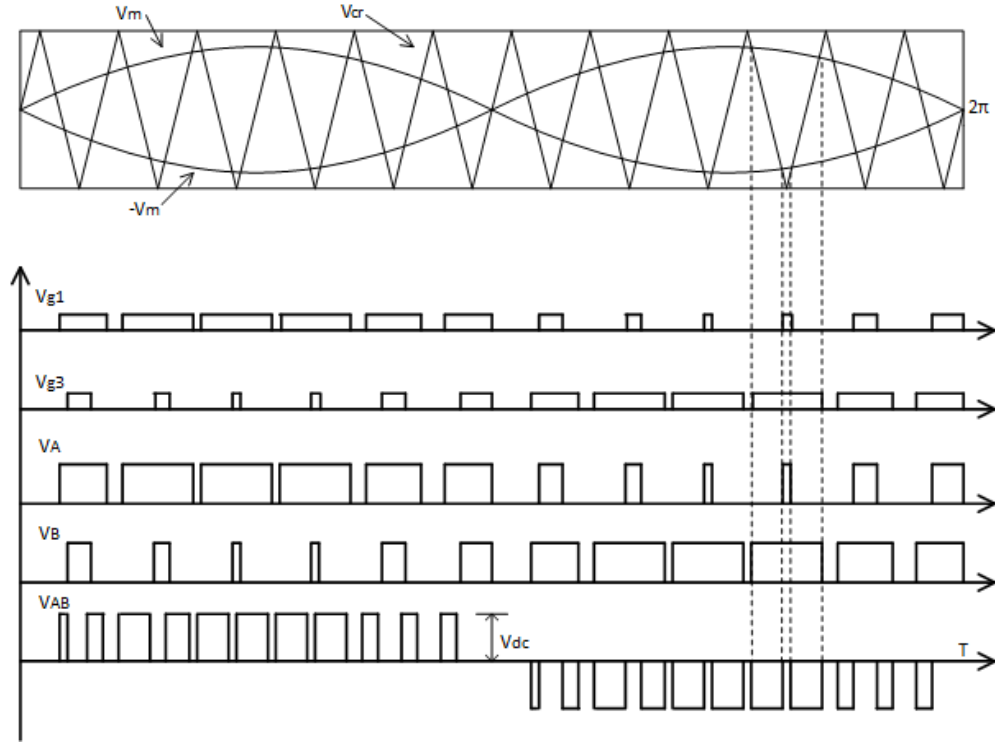


Figure 3.6 Schematic of unipolar PWM switching pattern

As we can see in Fig 3.6, V_m and $-V_m$ are modulating waves with same magnitude and 180° phase shift. The frequency of $\pm V_m$ are same as power frequency. V_{cr} is compared with two modulating waves to generate switching signals of switches. In Fig 3.6, switching signals of S1 and S3 are displayed. For switching signals of S2 and S4, they are complementary with switching signals of S1 and S3, respectively. Switching losses in this topology is same as bipolar PWM modulation since all the switches are operating at the carrier frequency.

Actually, switches S1 and S2 do not need to turn on or off at carrier frequency while maintain same voltage output in Fig. 3.6. In order to reduce switching losses, switch S1 in positive half cycle is modulating same as figure 3.6 while turn off during negative half cycle. Switch S2 is working complementary with S1 in negative half cycle while turn off in positive half cycle. Switch S3 is operating same as Fig 3.6 in negative half cycle and turn off in positive cycle. S4 is modulating complementary with S3 in positive cycle and switching off in negative cycle. The modulating signal of each power switch is shown in Fig 3.7.

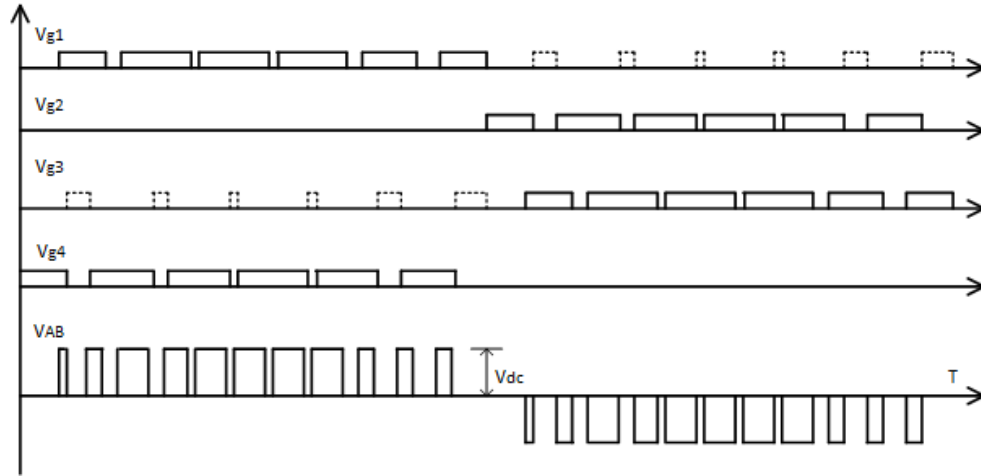


Figure 3.7 Unipolar PWM switching mechanism with reduced switching losses

As we can see in Fig 3.7, switching losses of improved unipolar PWM are reduced by half compared with original unipolar PWM. Total harmonic distortion of output voltage is lower than bipolar PWM since the output voltage switching times in one cycle of unipolar PWM are twice as switching times of bipolar PWM. In addition, the voltage amplitude difference of unipolar PWM is U_{dc} compared with $2U_{dc}$ in bipolar PWM. Consequently, large size inductor and capacitor

should be applied in inverter to reduce high current ripples in bipolar PWM schemes.

3.2.3 Simulation results of PV systems

(1) PV array Boost stage simulation

A schematic of PV array with boost converter is shown in Fig 3.8. As we discussed before, the DC voltage output of PV array cannot meet the requirement of grid standards. Therefore, a boost converter is applied to adjust voltage rating. Configurations and output data of PV array are listed in table 3.1. In this system, PV arrays are consisted of 10 series connected PV modules, and system ratings of PV array after boost converter are shown in Fig 3.9.

N_s (series connected PV modules)	10	$I_{pv}(A)$	3.56	$I_{dc}(A)$	2.44
N_p (parallel connected PV modules)	1	$V_{pv}(V)$	170	$V_{dc}(V)$	243.5
Testing condition	STC	$P_{in}(W)$	605.2	$P_{dc}(W)$	593

Table 3.1 Configurations and outputs of grid connected PV arrays

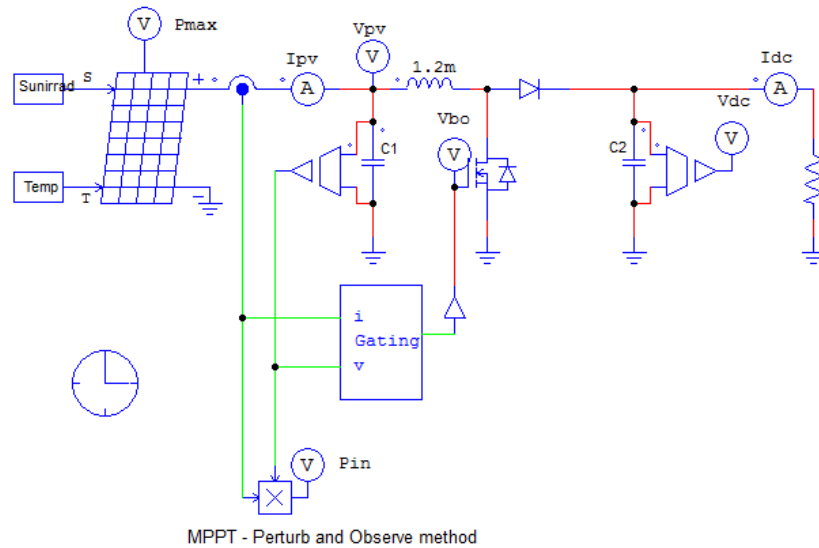


Figure 3.8 Schematic of PV array with Boost converter in PSIM

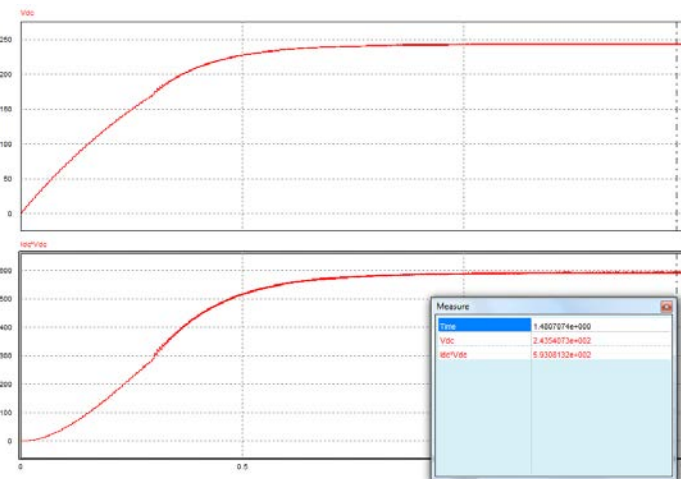


Figure 3.9 System rating at the output of boost converter

(2) Full bridge inverter

After getting the ideal voltage output from boost converter, a full bridge inverter is applied to generate sinusoidal signal and connected to the grid. Schematic of the full bridge inverter system is shown in Fig 3.10.

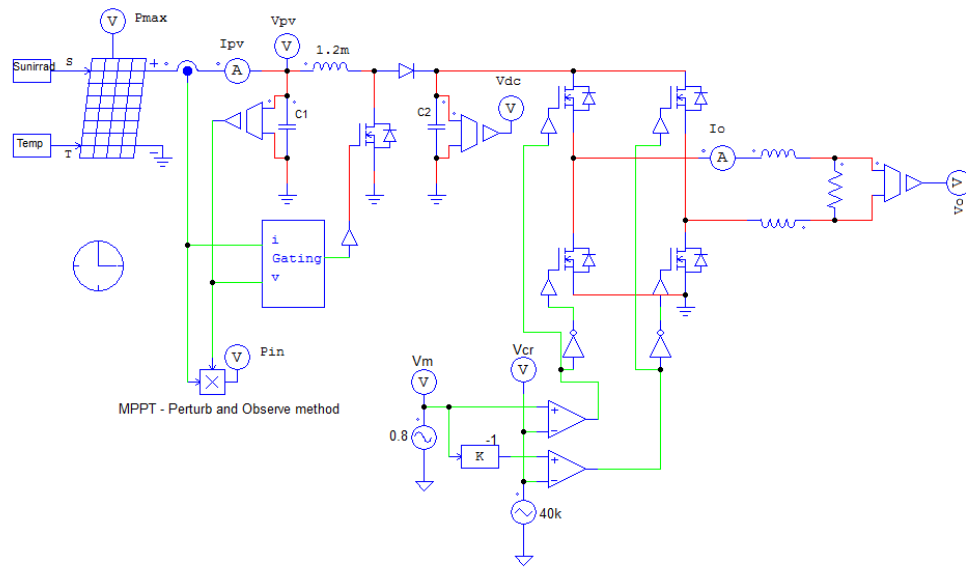


Figure 3.10 Schematic of single-phase grid connected full bridge inverter

Full bridge inverter was modulated by unipolar PWM. This modulation method generates output voltage and current with few ripple and requires small size LC filter to achieve sinusoidal voltage and current. RMS voltage, RMS current and power under this PV array configuration is 243V, 2.4A and 583W respectively (See Fig 3.11).

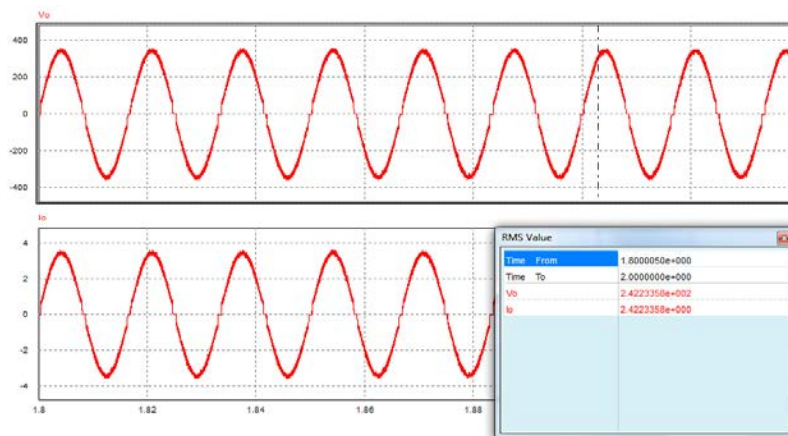


Figure 3.11 Voltage and current at the inverter output

3.2.4 Simplified model of ground fault analysis

Since we already described characteristics of PV arrays and boost converter, they can be modeled as a DC input voltage source. In order to achieve same current magnitude as PV array current in simplified model, equivalent load should be inserted at the grid side. Since this model shares same rating of power, output voltage and load current as practical model, it can represent all the relevant characteristics of original model. The simplified model of PV system is shown in Fig 3.12. This model is used to analyze DC side ground fault of single-phase PV system. Detection schemes of high impedance ground fault on PV arrays are proposed with this simplified model.

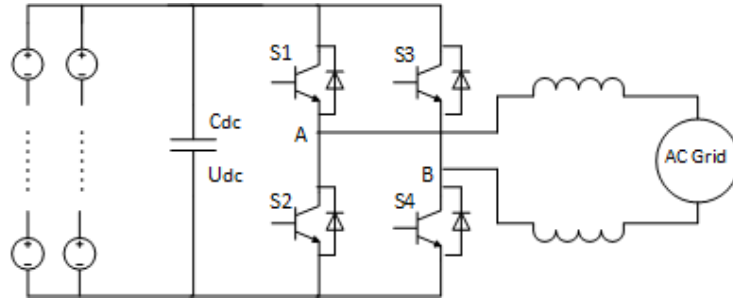


Figure 3.12 Simplified PV inverter model with DC source

3.3 Ground fault analysis in PV system

Ground faults can occur at any place of the PV system. However, most common locations of ground faults are at PV array, positive and negative power lines (See Fig. 3.13). In this section, we will simulate ground fault influences on system voltage and current at common locations. Table 3.2 summarizes magnitudes of ground fault current flows through GFDI.

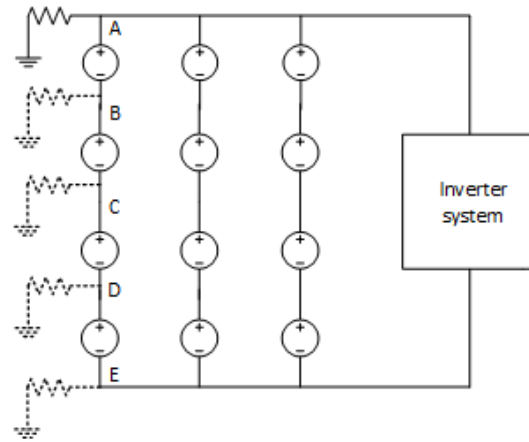


Figure 3.13 Illustration of fault locations

(1) Normal operation

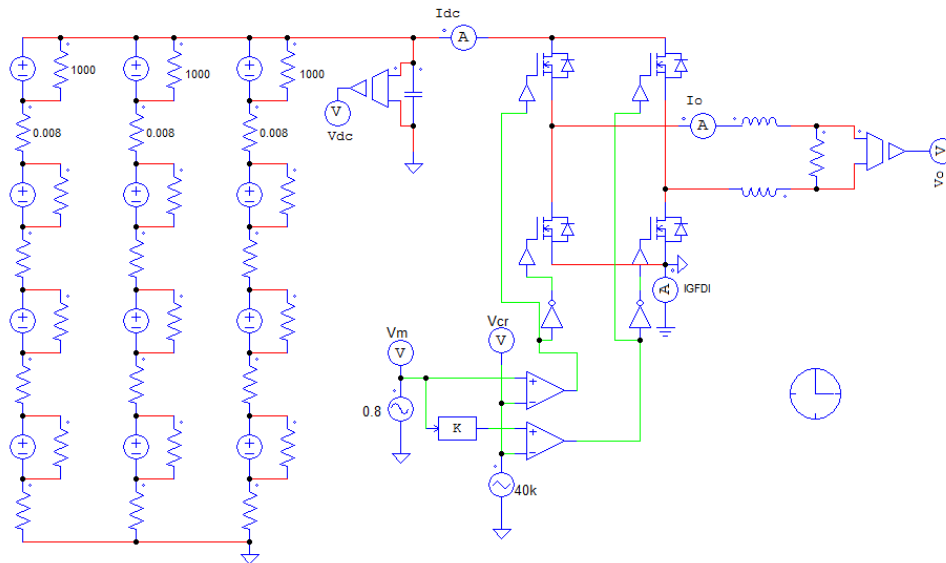


Figure 3.14 Schematic of normal operation

Fig. 3.14 describes the normal operation schematic of PV system. Current probe IGFDI is the modeled ground fault detection interrupter to measure

magnitude of current flows to ground. At this time, the fault current flows through GFID is zero.

(2) Positive power line ground fault

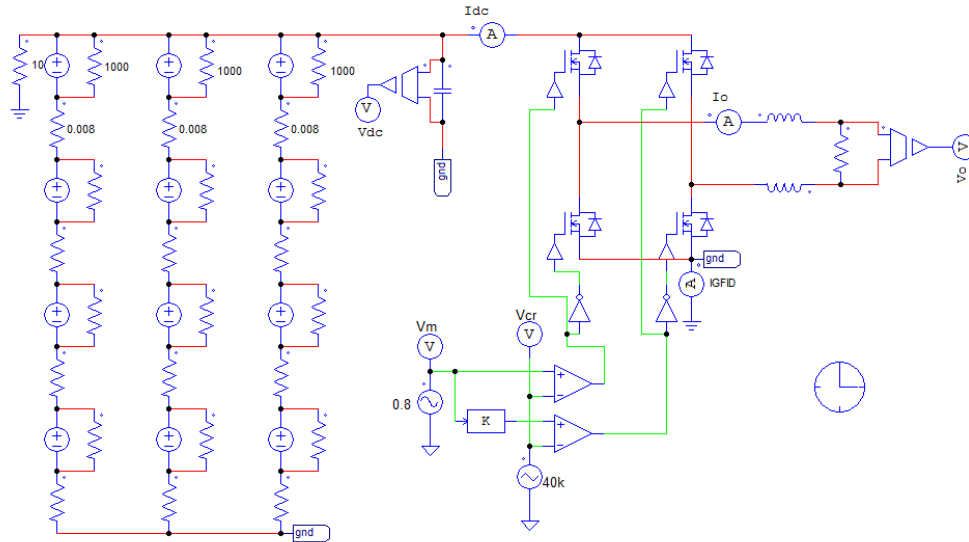


Figure 3.15 Schematic of ground fault at positive power line (A)

(3) Ground fault between PV arrays

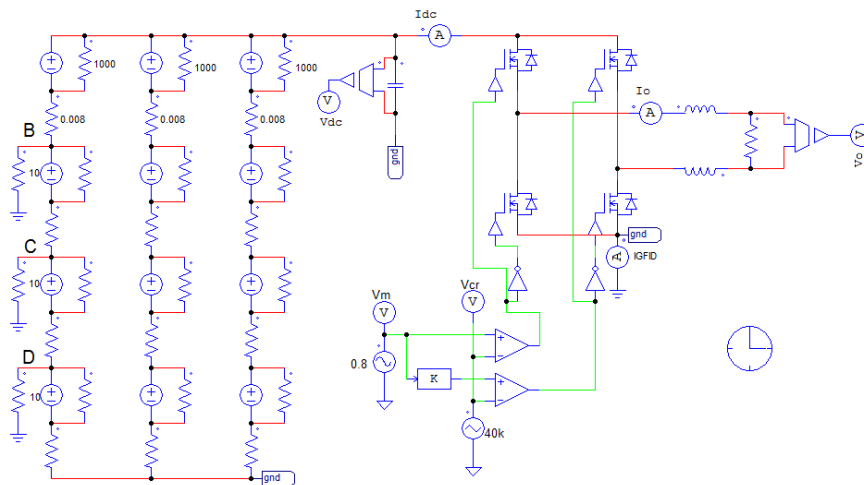


Figure 3.16 Schematic of ground fault between PV arrays (B, C, D)

(4) Negative power line ground fault

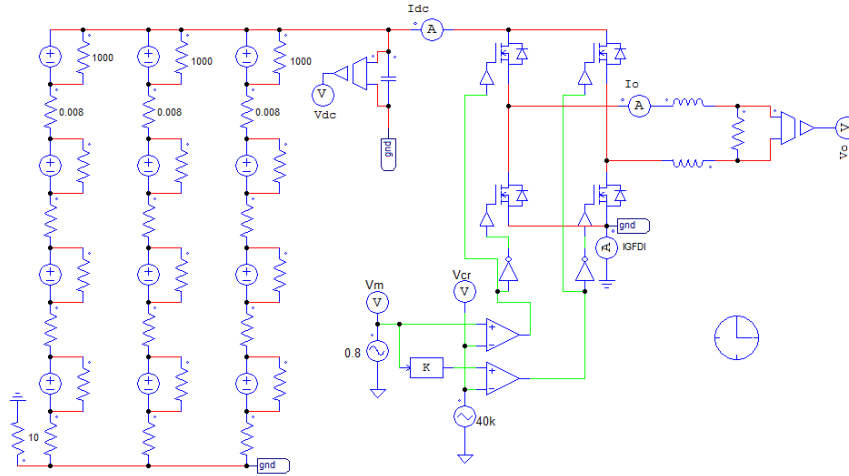


Figure 3.17 Schematic of ground fault at negative power line (E)

When ground faults occur at point A, B, C, and D, a fault current return path can be formed with a DC source, fault impedance and ground. However, when ground fault happens at point E, no obvious current will be detected since there is no DC power source between GFDI, fault impedance and ground.

Ground fault location	A	B	C	D	E
GFID current (A)	40	30	20	10	0

PV DC voltage: 400V Ground fault impedance: 10Ω

Table 3.2 Illustration of ground fault current flows through GFDI

3.4 Detection problems with high impedance ground fault

From section 3.3, it is easy to detect low impedance ground faults occur at PV arrays and positive power line. However, the current flow through of GFDI is not

enough to trigger interruption device and break the circuit in high impedance ground fault and negative power line ground fault conditions. In this section, we will analyze effectiveness of GFDI under high impedance ground fault and negative power line ground fault. Conclusion about detectable impedance of GFDI threshold at certain point is proposed in this section.

According to the data sheet of Outback PV Ground-Fault Detector Interrupter [36], the minimum current that flows through this device is 0.5A to trigger GFDI. With this minimum current threshold, corresponding ground fault impedances are listed at different locations of PV array in Table 3.3.

Ground fault location	A	B	C	D	E
Impedance threshold (Ω)	800	600	400	200	0

Table 3.3 Maximum impedance for indicating ground fault with Outback GFDI

Through analyzing the thresholds of ground impedance, GFDI can work normally for ground impedances under 500Ω at point A and B. In that case, no special device or method is needed for ground fault detection at A and B. For point C, D and E, no enough current will flow through GFDI if we have ground fault impedance greater than 400Ω . Therefore, an advanced method is required to detect high impedance ground fault and negative power line ground fault. Details of common mode method to identify high impedance ground fault or negative power line fault are discussed in Chapter 4.

CHAPTER 4: DC Side High Impedance

Ground Fault Detection

4.1 Common mode model of single-phase full bridge inverter

4.1.1 Common mode description of transformerless single-phase PV system

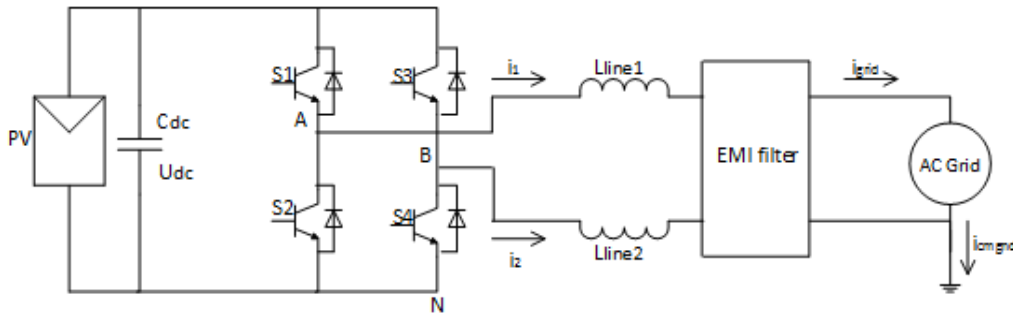


Figure 4.1 Scheme of single-phase transformerless PV inverter

Fig. 4.1 displays the general schematic of a single-phase transformerless PV system [37]. It consists of PV array, full bridge inverter, EMI filter and the electrical grid. PV arrays supply DC voltage to the inverter and the full bridge inverter modulates DC input voltage to create sinusoidal current that is injected into the grid. The EMI filter will confine high frequency noise magnitude to maintain normal operation of PV system.

Considering electromagnetic compatibility (EMC) of PV inverter system, common mode current needs to be carefully studied for normal operation of the PV system. However, common mode current is also a useful tool to analyze high impedance ground faults. We will introduce equations to express common mode

current and voltage and differential mode current and voltage. Effects of ground fault on common mode current will be discussed in the fourth section of this chapter.

Points A and B are output terminals of full bridge inverter and point N is the negative terminal of PV array. Common mode output voltage is usually described as average value between output terminals A, B, and reference node N. In Fig. 4.1, we can express common mode voltage as:

$$U_{cm} = \frac{U_{AN} + U_{BN}}{2} \quad (\text{Eq. 4.1})$$

Differential voltage is the difference between output terminals A, B, and reference node N:

$$U_{dm} = U_{AN} - U_{BN} \quad (\text{Eq. 4.2})$$

Similarly, output currents can also be written as common mode and differential mode expressions based on the reference node and output terminals. Under this configuration, common mode current can be defined as:

$$i_{cm} = i_1 + i_2 \quad (\text{Eq. 4.3})$$

Differential current can be defined as:

$$i_{dm} = \frac{i_1 - i_2}{2} \quad (\text{Eq. 4.4})$$

Ground current i_{cmgnd} in this figure shares the same magnitude as common mode current. If a common mode current is to circulate in the system, a return

loop, which usually consists of parasitic components, should be established. Therefore, common mode current can reflect the stray components' influence on the PV system. Since no return path is created for common mode current, i_{cmgnd} , it flows back to full bridge inverter, and i_{cm} equals zero and only differential current i_{dm} will feed to the grid.

4.1.2 Common mode model of transformerless single-phase PV system with stray components

The transformerless topology is adopted in the PV generation system. Therefore, a galvanic connection appears between PV array and the grid [38]. Scheme of the single-phase transformerless PV inverter with stray components are shown in Fig 4.2.

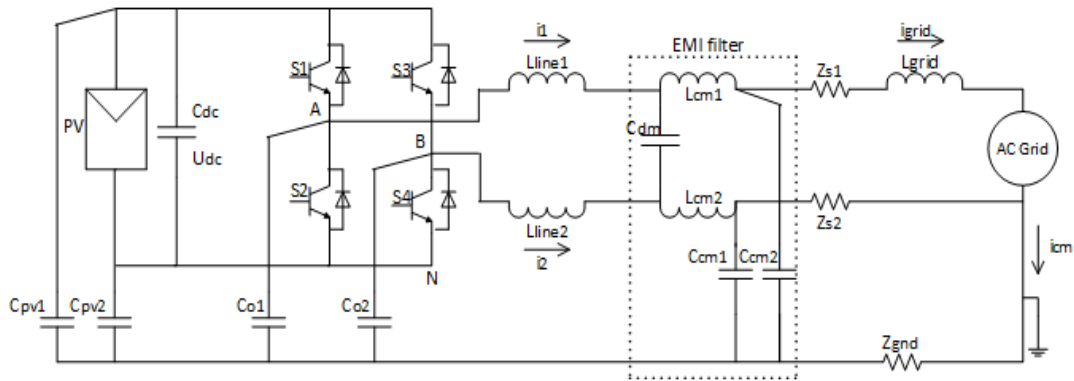


Figure 4.2 Scheme of single-phase transformerless PV inverter with stray components

Common mode parameters of PV system:

C_{pv1}, C_{pv2} : Stray capacitance between PV arrays and ground

C_{o1}, C_{o2} : Stray capacitance between PV inverter and ground

C_{cm1}, C_{cm2} : Common mode capacitance between EMI filter and ground

C_{dm} : Differential mode capacitance of EMI filter

L_{grid} : Grid series stray inductor

L_{line1}, L_{line2} : Line filter inductor for grid current

L_{cm1}, L_{cm2} : Common mode inductance of EMI filter

Z_{s1}, Z_{s2} : Grid series stray resistance

Z_{gnd} : Ground series resistance

With the path created by stray components, common mode current i_{cm} can flow through the parasitic elements, full bridge inverter and EMI filter and then feed to the grid. Past research [38] suggests that common mode current i_{cm} contains spectral information on fundamental components at grid frequency, medium frequency components at switching frequency and high frequency components spanning from 150kHz to 30MHz.

Frequency band flows follow different paths in the PV system. For the low frequency band components, common mode current is flowing through stray capacitor that is between PV arrays and ground, and grid ground impedance. This information will be magnified in large scale PV arrays due to increased stray capacitance of PV arrays. For the high frequency band components, common mode current is circulating between PV arrays to ground stray capacitor, inverter to ground capacitor and capacitive path of EMI filter. High frequency components will be limited by the EMI filter. The most significant information in common mode current is medium frequency component. Medium frequency components of

common mode current will flow through PV arrays to ground capacitance, inverter to ground capacitance, EMI filter capacitive path and ground series impedance.

The common mode model of PV system includes the common mode voltage source, PV arrays to ground capacitance, inverter to ground capacitance, common mode components of EMI filters, line inductance and ground impedance. All of these elements will affect the frequency response of common mode current. If high impedance ground fault works as part of common mode model, it will change the frequency characteristic of common mode current. This idea is utilized here to detect high impedance ground fault without any expensive instrumentation and additional system components.

The full bridge inverter functions as a discrete voltage generator in the PV system. It changes the DC voltage of PV output to certain switching patterns. We can represent the functions of PV arrays, full bridge inverter as two separate voltage source, which are denoted by U_{AN} and U_{BN} . A schematic of the PV system with two separate voltage sources is shown in Fig. 4.3.

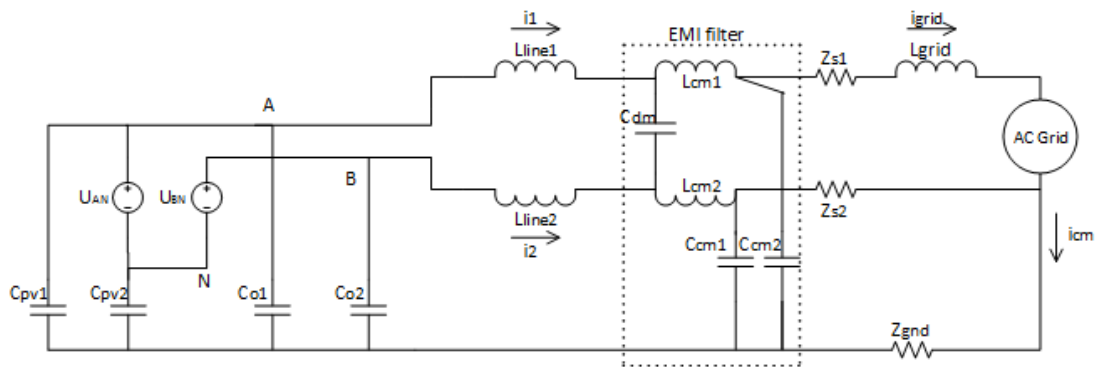


Figure 4.3 Schematic of PV system model with separate voltage sources

According to the equations of common mode voltage and differential voltage, U_{AN} and U_{BN} can be expressed as:

$$U_{AN} = U_{cm} + \frac{U_{dm}}{2} \quad (\text{Eq. 4.5})$$

$$U_{BN} = U_{cm} - \frac{U_{dm}}{2} \quad (\text{Eq. 4.6})$$

Applying U_{AN} and U_{BN} with common mode and differential mode equations into Fig. 4.3, new schematic is shown in Fig. 4.4.

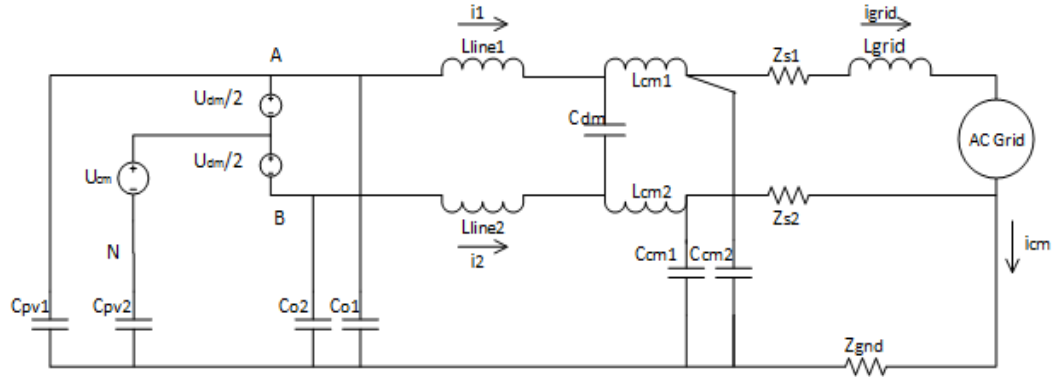


Figure 4.4 Schematic of PV system model with common and differential voltage sources

Since we are establishing the common mode model at switching frequency, grid has frequency between 50 to 60 Hz and can be removed due to insignificant impact on the frequency response of common mode current. The model without grid can only be applied in common mode analysis of system response. If we assume that stray capacitances between positive terminal of PV arrays and ground, and negative terminal of PV arrays and ground are the same ($C_{pv1} = C_{pv2}$), then schematic of Fig. 4.4 can be simplified as Fig. 4.5.

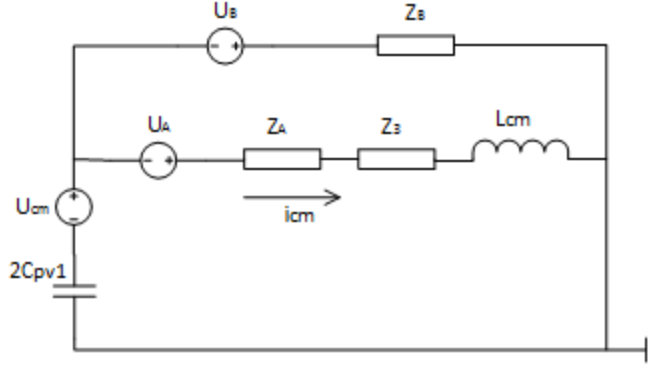


Figure 4.5 Schematic of simplified PV system common mode model

$$U_A = \frac{U_{dm}}{2} \frac{(Z_{line2} + Z_2) - (Z_{line1} + Z_1)}{Z_{line1} + Z_{line2} + Z_1 + Z_2} \quad (\text{Eq. 4.7})$$

$$Z_A = \frac{(Z_{line1} + Z_1)(Z_{line2} + Z_2)}{Z_{line1} + Z_{line2} + Z_1 + Z_2} \quad (\text{Eq. 4.8})$$

$$U_B = \frac{U_{dm}}{2} \frac{Z_{o2} - Z_{o1}}{Z_{o1} + Z_{o2}} \quad (\text{Eq. 4.9})$$

$$Z_B = \frac{Z_{o1} Z_{o2}}{Z_{o1} + Z_{o2}} \quad (\text{Eq. 4.10})$$

$$L_{cm} = L_{cm1} \parallel L_{cm2} \quad (\text{Eq. 4.11})$$

Z_1 , Z_2 , Z_3 in above equations are equal to listed value below:

$$Z_1 = \frac{Z_{s1} Z_{Ccm1}}{Z_{s1} + 2Z_{gnd} + Z_{Ccm1}} + \frac{2Z_{s2} Z_{gnd} Z_{Ccm1} + 2Z_{s1} Z_{gnd} Z_{Ccm1} (Z_{s2} + 2Z_{gnd} + Z_{Ccm2}) / (Z_{s1} + 2Z_{gnd} + Z_{Ccm1})}{(Z_{s1} + Z_{Ccm1})(Z_{s2} + 2Z_{gnd} + Z_{Ccm2}) + (Z_{s2} + Z_{Ccm2})(Z_{s1} + 2Z_{gnd} + Z_{Ccm1})}$$

$$Z_2 = \frac{Z_{s2}Z_{Ccm2}}{Z_{s2} + 2Z_{gnd} + Z_{Ccm2}} + \frac{2Z_{s1}Z_{gnd}Z_{Ccm2} + 2Z_{s2}Z_{gnd}Z_{Ccm2}(Z_{s1} + 2Z_{gnd} + Z_{Ccm1})/(Z_{s2} + 2Z_{gnd} + Z_{Ccm2})}{(Z_{s1} + Z_{Ccm1})(Z_{s2} + 2Z_{gnd} + Z_{Ccm2}) + (Z_{s2} + Z_{Ccm2})(Z_{s1} + 2Z_{gnd} + Z_{Ccm1})}$$

Z_3

$$= \frac{2Z_{Ccm1}Z_{Ccm2}Z_{gnd}}{(Z_{s1} + Z_{Ccm1})(Z_{s2} + 2Z_{gnd} + Z_{Ccm2}) + (Z_{s2} + Z_{Ccm2})(Z_{s1} + 2Z_{gnd} + Z_{Ccm1})}$$

Clearly, the grid impedance increases system complexity. Since grid impedance Z_{s1} and Z_{s2} are comparatively smaller than the line inductor, EMI filter parameters and stray capacitance between PV system and ground, we can remove the grid impedance for simple calculation and analysis ($Z_{s1}, Z_{s2} \approx 0$). For stray capacitances between switching legs and ground, symmetric property can be achieved by fine selection of switches and careful placement of full bridge inverter ($Z_{o1} = Z_{o2}$). We can neglect the effect of voltage source U_A in common mode model if two grid current inductors are identical on positive and negative power lines ($Z_{line1} = Z_{line2}$). Finally, we can get the schematic of common mode model of single-phase PV system in Fig. 4.6 with least number of stray parameters and contains all relevant information of system common mode response.

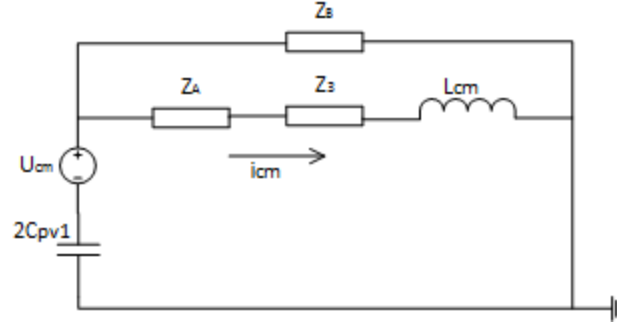


Figure 4.6 Final common mode model of single-phase transformerless PV system

$$Z_A = \frac{Z_{line1} * Z_{line2}}{Z_{line1} + Z_{line2}} \quad (\text{Eq. 4.12})$$

$$Z_B = \frac{Z_{o1} * Z_{o2}}{Z_{o1} + Z_{o2}} \quad (\text{Eq. 4.13})$$

$$Z_3 = \frac{Z_{Ccm1} Z_{Ccm2} Z_{gnd}}{Z_{gnd}(Z_{Ccm1} + Z_{Ccm2}) + Z_{Ccm1} Z_{Ccm2}} \quad (\text{Eq. 4.14})$$

4.2 Parameter estimation of PV systems

4.2.1 Common mode voltage source

Common mode voltage source is determined by magnitude of DC input voltage and PWM modulation method. Since we are adopting unipolar PWM switching pattern in this system, variable common mode voltage source is described in Fig. 4.7.

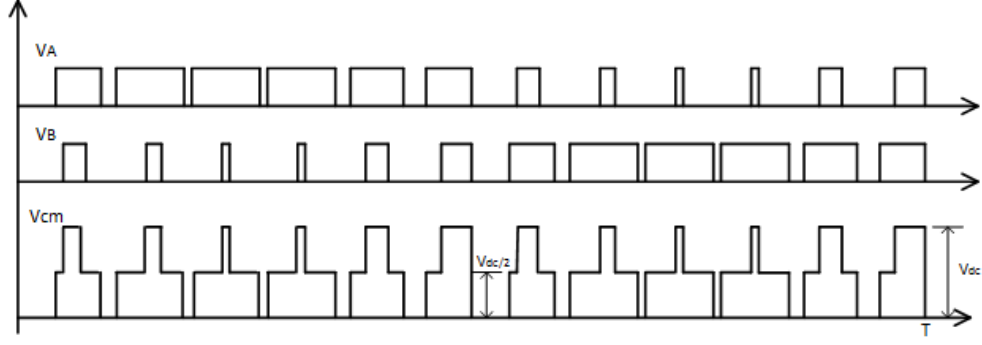


Figure 4.7 Common mode voltage scheme with unipolar PWM in full bridge inverter

4.2.2 Common mode stray parameters and grid current inductor

According to the proposed model in Fig. 4.6, common mode current is relevant to the stray capacitance between PV arrays and ground (C_{pv1}, C_{pv2}), and between PV inverter and ground (C_{o1}, C_{o2}), and common mode EMI capacitance between EMI filter and ground (C_{cm1}, C_{cm2}), grid current filter inductor (L_{line1}, L_{line2}), common mode inductance of EMI filter (L_{cm1}, L_{cm2}) and ground series resistance (Z_{gnd}). However, the values of these parameters are not obvious. Careful study and determination of these parameters helps us understand and get the accurate result of common mode current analysis.

According to [39], the leakage capacitance between PV arrays and ground (C_{pv1}, C_{pv2}) are influenced by PV panels and frame structures, surface of cells and distance between cells, module frame, weather conditions, humidity and dust covering the PV panels. Papers in [40][41] introduce the normal magnitude of PV arrays to ground capacitance in the PV system. For a PV module with nominal power 20W, it has parasitic capacitance around 73pF [40]. For large ungrounded

PV arrays, typical capacitance of PV arrays has found between 50 and 150nF/kW, and up to 1uF/kW in damp or rainy environments. If we have a PV system with 600W power output, we can estimate $2C_{pv1}$ in this system is from 30 to 90nF.

The stray capacitance between PV inverter and ground (C_{o1}, C_{o2}) depends on the connection between the switch legs and grounded heatsink. For a 1 kW power inverter, parasitic capacitance to ground is 150pF through measurement of precision RLC meter [40]. Our system can generate output power of 600W. Accordingly, the magnitude of PV inverter to ground capacitance is set to 45pF (C_{o1}, C_{o2}).

EMI filter is adopted in the PV system to reject high frequency components of common mode current. However, EMI filter will induce common mode inductance and common mode capacitance. As we discussed before, stray capacitance of common mode filter will change the characteristic of common mode current and common mode inductance of EMI filter will change the total impedance of common mode model. For small power output PV systems, common mode inductances (L_{cm1}, L_{cm2}) and common mode capacitances (C_{cm1}, C_{cm2}) of the EMI filter are 2mH and 3nF, respectively.

The ground series impedance (Z_{gnd}) represents inductive characteristic between ground connection points of converter and the grid. Normally, this impedance is nearly equal to zero and we can neglect the influence of ground impedance in our analysis of common mode behavior. A summary of all the parameters in this common mode model is displayed in Table 4.1.

L_{line1}, L_{line2}	C_{pv1}, C_{pv2}	L_{cm1}, L_{cm2}	C_{cm1}, C_{cm2}	C_{o1}, C_{o2}	Z_{gnd}
2 mH	15 nF	2 mH	3 nF	45 pF	0

Table 4.1 Common mode model parameters for PV system

4.3 Resonant frequency analysis of common mode current

Since we have derived common mode model and parameters of the single-phase PV system, electrical circuits and the simulation model are established and studies can be conducted to evaluate the influences of stray components on common mode currents.

According to the parameters selected for PV system, magnitudes of Z_A , Z_B , L_{cm} and Z_3 are listed below:

$$Z_A = \frac{Z_{line1} * Z_{line2}}{Z_{line1} + Z_{line2}} = 1\text{mH}$$

$$Z_B = \frac{Z_{o1} * Z_{o2}}{Z_{o1} + Z_{o2}} = 90\text{pF}$$

$$Z_3 = \frac{Z_{Ccm1}Z_{Ccm2}Z_{gnd}}{Z_{gnd}(Z_{Ccm1} + Z_{Ccm2}) + Z_{Ccm1}Z_{Ccm2}} = 0$$

$$L_{cm} = L_{cm1} \parallel L_{cm2} = 1\text{mH}$$

4.3.1 Simplified common mode model simulation

(1) U_{cm} with constant DC voltage

Firstly, we will simulate the simplified circuit with constant DC voltage source. The simulation result with DC input common mode voltage source will help us understand full bridge inverter with bipolar PWM switching technique. For the bipolar PWM switching method, the common mode output voltage will not vary significantly and magnitude of common mode voltage is equal to half of the DC input voltage. Resonant frequency of common mode current in this case is generated by stray parameters of common mode model and resonant frequency information will not reflect switching characteristic of the full bridge inverter. In Fig. 4.8, we will replace the variable common mode voltage source with 200V DC source.

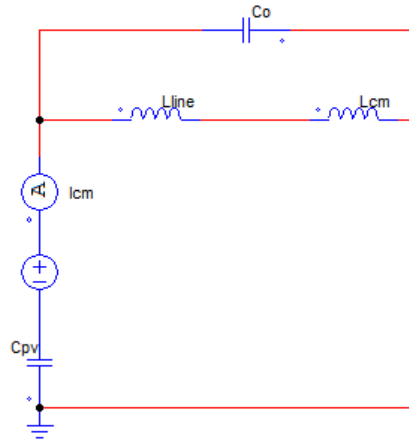


Figure 4.8 Simplified model with constant CM voltage source

Equation describing the impedance of this simplified common model can be derived from Fig. 4.8:

$$Z_1 = j\omega(L_{Line} + L_{cm}) \parallel \frac{1}{j\omega C_o} + \frac{1}{j\omega C_{pv}} = \frac{-j[1-\omega^2(L_{Line}+L_{cm})(C_o+C_{pv})]}{[1-\omega^2(L_{Line}+L_{cm})C_o]\omega C_{pv}} \quad (\text{Eq. 4.15})$$

If we want to reach the minimum value of circuit impedance, ω can be made equal to ω_1 . At this point, the total impedance of common mode model is zero, and resonant common mode current can be found at ω_1 (See Fig. 4.9).

$$\omega_1 = \sqrt{\frac{1}{(L_{Line}+L_{cm})(C_o+C_{pv})}} \quad (\text{Eq. 4.16})$$

$$f_1 = \frac{1}{2\pi} \sqrt{\frac{1}{(L_{Line}+L_{cm})(C_o+C_{pv})}} \quad (\text{Eq. 4.17})$$

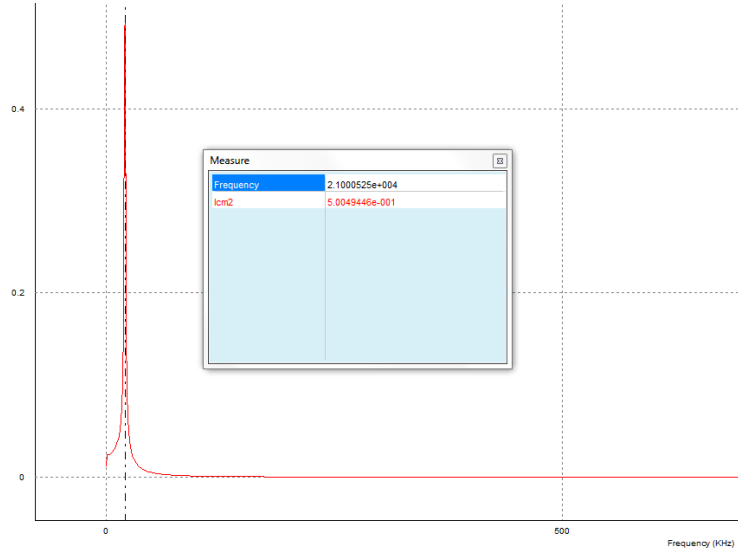


Figure 4.9 Common mode current at resonant frequency

According to the estimated parameters in section 4.2.2, the resonant frequency equals to 20.52 kHz. The circuit simulation validates the calculated resonant frequency location. The magnitude of common mode current at resonant frequency is 0.5A.

(2) U_{cm} with unipolar PWM switching

The DC common mode voltage source is replaced by voltage source modulated with unipolar PWM technique. With this variable voltage source, we can expect the frequency response of common mode current to contain information about more than just the resonant frequency with DC input source. Fig. 4.10 displays the schematic of simplified model with variable input voltage source and Fig. 4.11 shows the common mode current spectrum.

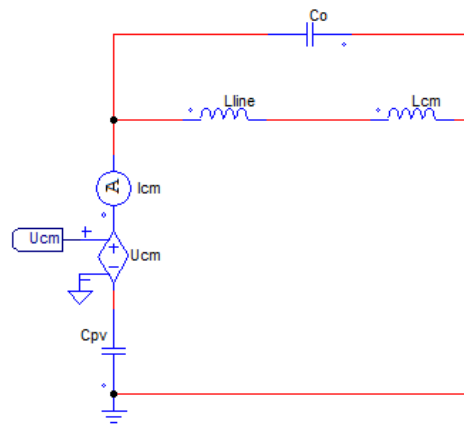


Figure 4.10 Simplified model with unipolar PWM switching CM voltage source

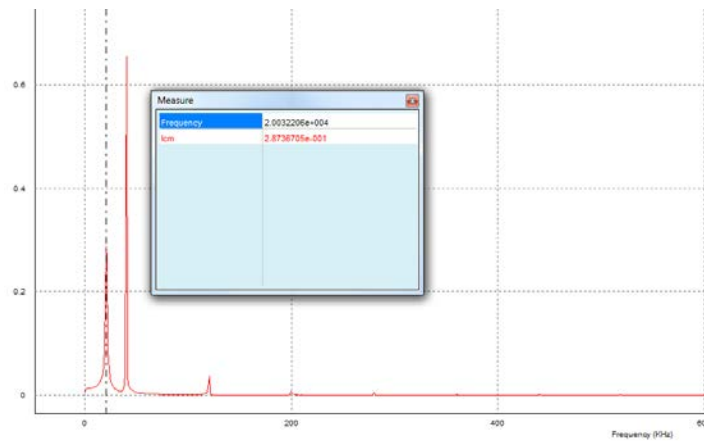


Figure 4.11 Common mode current at resonant frequency

Form the common mode current spectrum, resonant frequency will exist at 20.03 kHz. However, due to the variable characteristic of the common mode voltage source, resonant frequencies can also be found at odd multiples of the switching frequency. The magnitude of common mode current which reflects stray parameter characteristic is 0.29A.

4.3.2 Common mode analysis of PV system with stray parameters

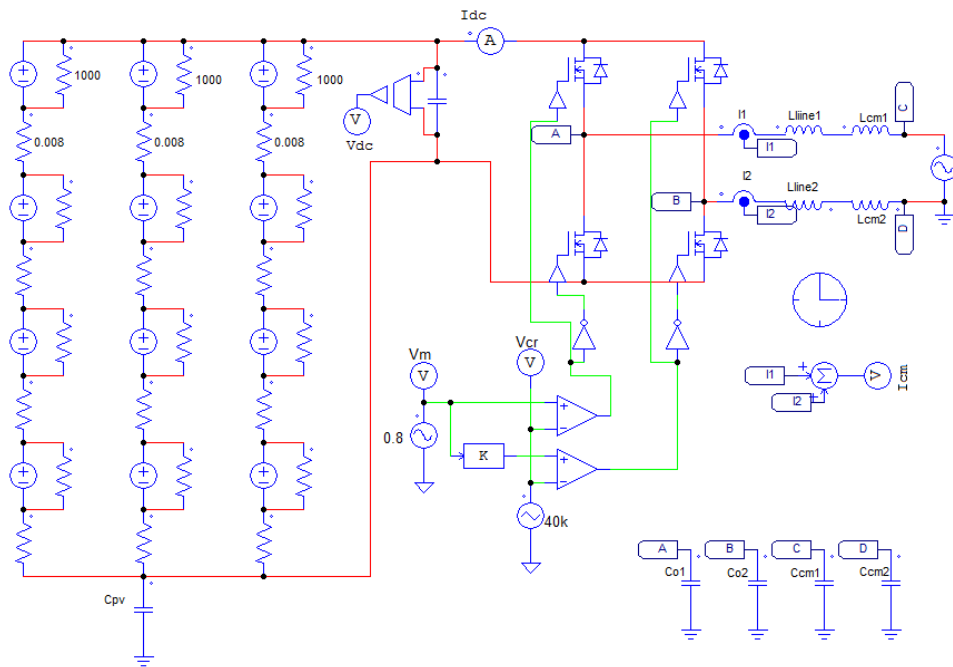


Figure 4.12 Full bridge inverter with stray parameters

In order to verify our derived simplified common mode model of the PV system, full bridge circuit with stray parameters is simulated in PSIM environment. Fig. 4.12 shows the schematic of PV system with stray parameters and Fig. 4.13 illustrates common mode current spectrum under this configuration.

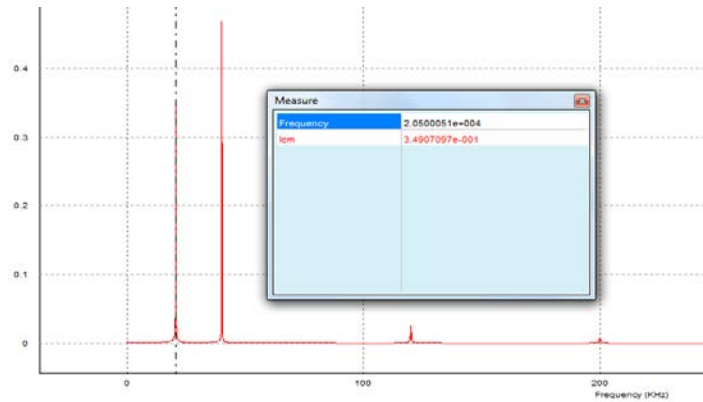


Figure 4.13 Spectrum of common mode current with full bridge inverter

From Fig. 4.13, the resonant frequency is located at 20.50 kHz and magnitude of common mode current at this frequency is 0.35A. We can compare this frequency location with simplified model of variable voltage source and DC voltage source. All of these three models have resonant frequency band between 20 kHz and 21 kHz. Common mode current spectrum in this figure also shows odd order harmonics of switching frequency, which is same as simplified model with variable voltage source. Table 4.2 summarizes resonant current magnitudes and their corresponding frequency locations.

Simulation model type	Simplified circuit with DC voltage source	Simplified circuit with CM voltage source	Full bridge inverter with stray parameters
Resonant frequency location (kHz)	21.00	20.03	20.50
Current at resonant frequency (A)	0.50	0.29	0.35

Table 4.2 Resonant frequency information of different simulation models

According to the summary of resonant frequency locations and magnitudes, we can conclude the single-phase transformerless PV system with 600W power output will have common mode current resonant frequency between 20 kHz and 21 kHz during normal operation. This characteristic will be influenced by ground fault since ground fault changes the common mode model impedance. Details about high impedance ground fault common mode features will be analyzed in the next section.

4.4 HIGF detection with resonant frequency spectrum

PV arrays with accidental contact to the ground are possible hazards if the ground fault is not detected and removed in time. Recalling our discussion from Chapter 3, the ground impedance can vary from near zero to kilo ohms. GFDI can detect low impedance ground faults at the positive power line and between PV modules. However, for high impedance ground fault between PV modules and even low impedance at negative power line, GFDI is not very effective in actual application. Here, we will take advantage of the common mode characteristic of PV system to detect the high impedance ground faults at all locations.

4.4.1 HIGF detection in simplified common mode model

(1) U_{cm} with constant DC voltage

In Fig. 3.13, it displays possible locations of ground fault. The ground fault at each location will involve parallel connection with parasitic capacitance between PV array and ground, see Fig. 4.14. The parallel connection of ground fault and stray capacitance will change the total impedance of common mode model.

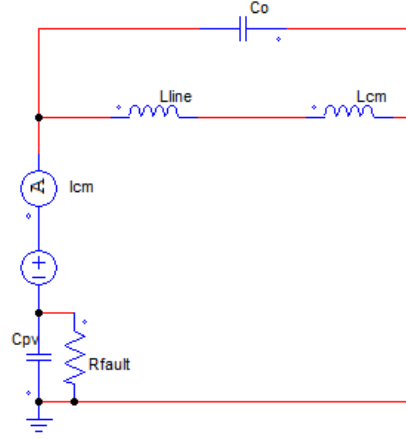


Figure 4.14 DC voltage source common model with HIGF

$$\begin{aligned}
 Z_2 &= j\omega(L_{Line} + L_{cm}) \parallel \frac{1}{j\omega C_o} + \frac{1}{j\omega C_{pv}} \parallel R_{fault} \\
 &= \frac{R_{fault}}{1 + \omega^2 C_{pv}^2 R_{fault}^2} + j \left[\frac{\omega(L_{Line} + L_{cm})}{1 - \omega^2 C_o(L_{Line} + L_{cm})} - \frac{\omega C_{pv} R_{fault}}{1 + \omega^2 C_{pv}^2 R_{fault}^2} \right]
 \end{aligned}$$

(Eq. 4.18)

Fig. 4.15 illustrates common mode current with 400 ohms of ground fault.

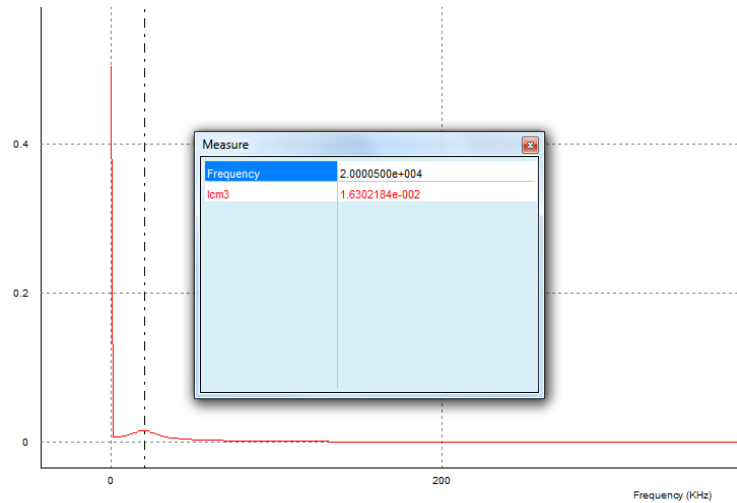


Figure 4.15 Common mode current spectrum with 400 ohms ground fault (DC source)

As we can see from the common mode current spectrum, resonant frequency location moves lower point, and the original resonant frequency (20 kHz) will only have current magnitude of 0.016A. Different magnitudes of ground faults will be simulated, and magnitudes of CM currents at original resonant frequency are recorded in Table 4.3.

Ground impedance (ohm)	Normal	400	800	2000
Resonant current magnitude (A)	0.50	0.016	0.036	0.088

Table 4.3 Resonant current at normal resonant frequency (20 kHz) with HIGF (DC source)

From simulation results of common mode model with DC voltage source, common mode current at original resonant frequency will be decreased compared

with normal operation. HIGF with 2000 ohms will only have the magnitude of common mode resonant current less than 1/5 of normal operation.

(2) U_{cm} with unipolar PWM switching

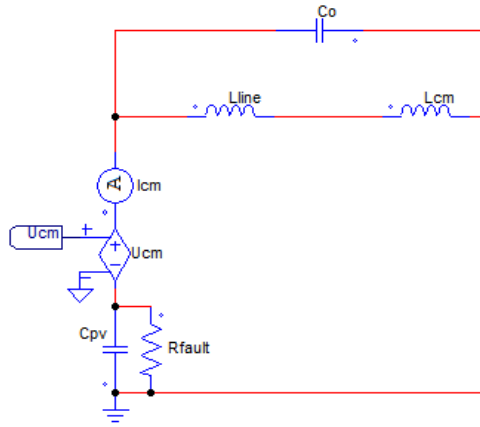


Figure 4.16 CM voltage source model with HIGF

Fig. 4.16 shows the schematic of common mode variable voltage source model with HIGF parallel connected to the stray capacitance between PV array and ground. The common mode current at original resonant frequency with 400 Ohms HIGF is displayed in Fig. 4.17.

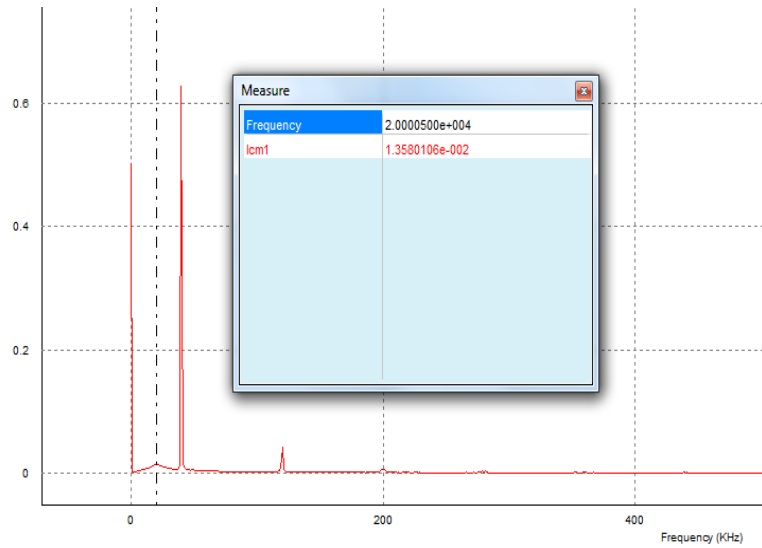


Figure 4.17 Common mode current spectrum with 400 ohms ground fault (CM voltage source)

Common mode current at original resonant frequency (20 kHz) is dropping to 0.014A compared with 0.29A for normal operation. Updated resonant frequency will again decrease. Influences of different magnitudes of fault impedance to common mode current at original frequency are displayed in Table 4.4.

Ground impedance (ohm)	Normal	400	800	2000
Resonant current magnitude (A)	0.29	0.014	0.022	0.050

Table 4.4 Resonant current at normal resonant frequency (20 kHz) with HIGF (CM voltage source)

Simulation results in this case further prove that HIGF in PV arrays will decrease the magnitude of common mode current at original resonant frequency

(20 kHz). The magnitude of resonant current at 20 kHz with 2000 ohms HIGF is only 1/6 of the current in the normal operation.

4.4.2 HIGF common mode analysis of PV system with stray parameters

Fig. 4.18 illustrates the full bridge PV system with stray parameters. HIGF can possibly occur at power lines or connections between PV arrays. In addition, the magnitude of ground fault impedance varies significantly. Ground faults at different locations and different magnitudes of impedance are simulated below. According to the common mode current spectrum, magnitudes of the resonant current with different ground impedances at different locations are recorded in Table 4.5. From the data of common mode current responses, HIGF can affect resonant common mode current magnitudes at all possible locations of PV arrays. The ground fault can be detected using common mode current characteristics of PV systems.

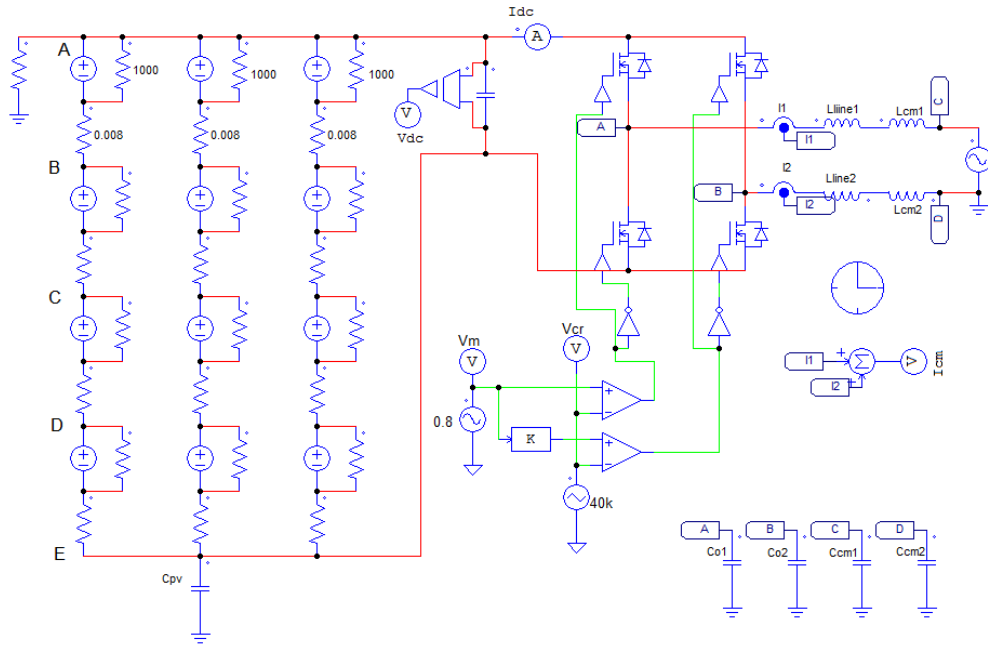


Figure 4.18 HIGF operations of full bridge inverter with stray parameters

Fault impedance Fault location	400 Ω	800 Ω	2000 Ω	Normal ($+\infty$)
A	0.001	0.002	0.005	0.349
B	0.001	0.002	0.005	0.349
C	0.001	0.002	0.005	0.349
D	0.002	0.002	0.005	0.349
E	0.002	0.003	0.005	0.349

Table 4.5 Resonant common mode current magnitude at 20 kHz (A)

Original PV system has the resonant frequency of common mode current around 20 kHz. The PV system with significant HIGF will reduce magnitude of

common mode current at original frequency location, and new resonant frequency is lowered.

4.5 Conclusion of HIGF detection with CM current method

According to the simulation results, HIGF can be reliably detected with the inspection of common mode current's resonant frequency. Both normal operation and HIGF operation are simulated under the situation of common mode model with DC voltage source, common mode model with variable voltage source and the single-phase full-bridge schematic with stray parameters. During normal operation of the PV system, common mode model with DC voltage source will have resonant frequency when the common mode model has lowest impedance. For common mode model with a variable input voltage source, current spectrum will not only contain the resonant frequency information, but also have odd harmonics of the switching frequency. Through the simulation of PV system with stray parameters, common mode current will have nearly the same resonant frequency as the simplified mode with voltage sources. These three tests verify the effectiveness of the common mode model and clarify influence of PV system's stray parameters on common mode current spectrum.

With the knowledge of common mode model and current resonant frequency characteristics, models with HIGF have been tested. The resonant frequency is reduced and the current magnitude at original resonant frequency location will drop to a significantly lower value in HIGF occasion. 2000 ohms of ground fault is simulated in three models, and all of these models will have a decreased

magnitude of current at original resonant location and new resonant points are all at lower frequencies. Different fault locations and different fault impedances are simulated in PV arrays. Testing results validate the reliability of common mode method to detect HIGF in PV systems.

Through analyzing common mode current spectrum in the PV system, we can design procedures to detect the high impedance ground fault. Firstly, we should find stray parameters since different PV systems will behave varied parasitic parameters. With the information about stray parameters, resonant frequency of the common mode current can be calculated and tested in the PV system. For a particular PV system, the resonant frequency location and magnitude of common mode current will not vary significantly during normal operation. However, when affected by HIGF, the common mode current spectrum is different. The magnitude of common mode current at normal resonant location is reduced and a new resonant frequency is reduced. Inspections of magnitude and location of common mode current will help us understand working condition of PV system and common mode measurements make possible a robust detection of HIGF at PV arrays.

CHAPTER 5: Conclusion and Future Work

5.1 Conclusion

An increasing number of PV generation plants has been built over the years, and the participation of solar energy in total generation shows a growing trend. In the first chapter of this this thesis, advantages of utilizing solar energy were discussed. However, some unresolved issues exist in the PV generation system that are slowing the development of PV industry. We are focusing on ground fault characteristics and detection techniques of the PV system.

At the beginning of Chapter 2, we introduce fundamental physical characteristics of solar cells. Elements, that influence the performance of solar cells, were discussed. Based on these factors, a mathematical model was presented to evaluate the relationship between solar cell's output current and voltage. The model is simulated in the PSIM environment, and the simulation result is compared with ideal model in PSIM. Our mathematical model effectively captures working properties of solar cells. Through the I-V curve of PV module output, an MPPT algorithm is typically implemented in the PV system in order to get the highest efficiency of PV modules. The temperature and sun irradiance are two most important ambient factors that will change the power output of PV modules. For discovering electrical characteristics of PV modules, series and parallel connections of PV modules are simulated in the PSIM environment. In Chapter 2, we derive an equation that describes effects of numbers of series and

parallel connected PV modules on the total power output of PV arrays. As expected, the MPP current is multiplied by the number of PV strings connected in parallel, and MPP voltage is multiplied by the number of PV modules connected in series on a single PV string. At the final part of this chapter, several commonly used PV module brands are introduced and their main applicable areas are discussed.

PV system usually consists of PV arrays, MPPT converter, inverter, transformer and grid. However, transformer is not an essential part of the PV system. Most advanced PV systems, especially in distributed power generation area, has already removed transformer to reach high converting efficiency, small size and easy transportation features. This system is implemented with PV arrays, boost converter, full bridge inverter and grid. The whole system with 600W power output is simulated, and performance is evaluated in PISM environment. Considering the ground fault is the one of the most common hazard in PV generation system, a GFDI is typically implemented to detect the hidden ground fault. In the special case of high impedance ground fault on the DC side of PV system, not enough current will flow through the GFDI to trigger the breaker.

In order to tackle the high impedance ground fault issue, a new method with common mode idea is presented in Chapter 4. In this chapter, the leakage current is introduced, which is related to stray parameters of the PV system. Leakage current can be represented by an equation connecting it with the common mode current. An equivalent model of common mode current is derived to simplify the

expression of full bridge common mode inverter. According to the common mode model, leakage current spectrum can be studied. However, ground faults in PV arrays will change the original pattern of common mode model impedances, and this idea is adopted to detect HIGF, since variation of common mode impedance will change common mode current spectrum. Through comparing and analyzing common mode model impedance of normal operation and HIGF operation, differences of common mode current resonant frequency and magnitude are investigated. By inspecting the differences between common mode current spectra, HIGF can be detected and removed in real time, which will maintain normal operation and guarantee safety of the PV system.

5.2 Future work

A new detection method has been discovered and verified in PSIM environment, and my future work includes applying the common mode current detection method into actual systems. In order to test common mode behavior, stray parameters should be examined and calculated carefully. These parameters vary with temperature, humidity and other factors. Numerous detection experiments should be conducted to establish empirical magnitudes of stray parameters based on system configurations and power output. Practical thresholds of resonant common mode current magnitude and resonant frequency can be derived to decide whether there exists a high-impedance ground fault in the PV system.

Bibliography

- [1] Schultz, O., et al. "Silicon solar cells with screen-printed front side metallization exceeding 19% efficiency." Proceedings of the 22nd European Photovoltaic Solar Energy Conference (PVSEC). 2007.
- [2] Dimroth, F. "World record solar cell with 44.7% efficiency." 2013-09-23)[2014-11-07]. [http://www.ise.fraunhofer.de/en/press-and-media/press-releases/presseinformationen-2013/world-record-solar-cell-with-44.7-efficiency\(2013\).](http://www.ise.fraunhofer.de/en/press-and-media/press-releases/presseinformationen-2013/world-record-solar-cell-with-44.7-efficiency(2013).)
- [3] Masson, Gaëtan, et al. "Global market outlook for photovoltaics 2013-2017." European Photovoltaic Industry Association (2013): 12-32.
- [4] PVPS, IEA. "PVPS Report—A Snapshot of Global PV—1992-2012." Report IEA-PVPS T1-22 2013 (2013).
- [5] Wilhelm, I., S. Teske, and G. Massonet. "Solar photovoltaic electricity empowering the world." Solar Gen 6 (2011): 17-28.
- [6] Shafiee, Shahriar, and Erkan Topal. "When will fossil fuel reserves be diminished?." Energy policy 37.1 (2009): 181-189.
- [7] Leckner, Bo. "The spectral distribution of solar radiation at the earth's surface—elements of a model." Solar energy 20.2 (1978): 143-150.
- [8] Green, Martin A., et al. "Solar cell efficiency tables (Version 45)." Progress in photovoltaics: research and applications 23.1 (2015): 1-9.
- [9] Alam, Mohammed Khorshed, et al. "PV faults: Overview, modeling, prevention and detection techniques." Control and Modeling for Power Electronics (COMPEL), 2013 IEEE 14th Workshop on. IEEE, 2013.
- [10] Ancuta, F., and C. Cepisca. "Fault analysis possibilities for PV panels." Energetics (IYCE), Proceedings of the 2011 3rd International Youth Conference on. IEEE, 2011.
- [11] Flicker, Jack, and Jay Johnson. "Electrical simulations of series and parallel PV arc-faults." 39th IEEE PVSC, Tampa (2013).
- [12] Alam, Mohammed Khorshed, et al. "PV arc-fault detection using spread spectrum time domain reflectometry (SSTD)." Energy Conversion Congress and Exposition (ECCE), 2014 IEEE. IEEE, 2014.
- [13] Johnson, Jay, et al. "Photovoltaic DC arc fault detector testing at Sandia National Laboratories." Photovoltaic Specialists Conference (PVSC), 2011 37th IEEE. IEEE, 2011.
- [14] Johnson, Jay, et al. "Creating dynamic equivalent PV circuit models with impedance spectroscopy for arc fault modeling." Photovoltaic Specialists Conference (PVSC), 2011 37th IEEE. IEEE, 2011.

- [15] Johnson, Jay, et al. "Using PV Module and Line Frequency Response Data to Create Robust Arc Fault Detectors." 26th European Photovoltaic Solar Energy Conference and Exhibition Hamburg, Germany. 2011.
- [16] Luebke, Charles, et al. "Field test results of DC arc fault detection on residential and utility scale PV arrays." Photovoltaic Specialists Conference (PVSC), 2011 37th IEEE. IEEE, 2011.
- [17] Johnson, Jay, et al. "Differentiating series and parallel photovoltaic arc-faults." Photovoltaic Specialists Conference (PVSC), 2012 38th IEEE. IEEE, 2012.
- [18] Braun, Henry, et al. "Signal processing for fault detection in photovoltaic arrays." Acoustics, Speech and Signal Processing (ICASSP), 2012 IEEE International Conference on. IEEE, 2012.
- [19] Li, Zhihua, et al. "An Intelligent Method for Fault Diagnosis in Photovoltaic Array." System Simulation and Scientific Computing. Springer Berlin Heidelberg, 2012. 10-16.
- [20] Zhao, Ye, et al. "Fault analysis in solar PV arrays under: Low irradiance conditions and reverse connections." Photovoltaic Specialists Conference (PVSC), 2011 37th IEEE. IEEE, 2011.
- [21] Zhao, Ye, et al. "Decision tree-based fault detection and classification in solar photovoltaic arrays." Applied Power Electronics Conference and Exposition (APEC), 2012 Twenty-Seventh Annual IEEE. IEEE, 2012.
- [22] Nelson, Jenny. The physics of solar cells. Vol. 57. London: Imperial college press, 2003.
- [23] Zhao, Ye. "Fault analysis in solar photovoltaic arrays." (2010).
- [24] Mboumboue, E., and D. Njomo. "Mathematical Modeling and Digital Simulation of PV Solar Panel using MATLAB Software." International Journal of Emerging Technology and Advanced Engineering 3.9 (2013): 24-32.
- [25] PSIM Tutorial. "How to Use Solar Module Physical model." Pwoersim Inc.
- [26] Solarex Manual. "MSX-60 and MSX-64 Photovoltaic Modules." www.solarex.com.
- [27] Esram, Trishan, and Patrick L. Chapman. "Comparison of photovoltaic array maximum power point tracking techniques." *IEEE TRANSACTIONS ON ENERGY CONVERSION* EC 22.2 (2007): 439.
- [28] Xiao, Weidong, and William G. Dunford. "A modified adaptive hill climbing MPPT method for photovoltaic power systems." *Power Electronics Specialists Conference, 2004. PESC 04. 2004 IEEE 35th Annual*. Vol. 3. Ieee, 2004.
- [29] Femia, Nicola, et al. "Optimization of perturb and observe maximum power point tracking method." *Power Electronics, IEEE Transactions on* 20.4 (2005): 963-973.
- [30] Liu, Fangrui, et al. "A variable step size INC MPPT method for PV systems." *Industrial Electronics, IEEE Transactions on* 55.7 (2008): 2622-2628.

- [31] KD315GX-LPB Solar Photovoltaic Power Modules. "Kyocera Installation Manual."
- [32] MaxPower CS6X 290/295/300/305/310M. "CanadianSolar Manual."
- [33] GS-S-390-TS High Efficiency Mono-crystalline Photovoltaic Module. "Grape solar Manual."
- [34] Kjaer, Soeren Baekhoej, John K. Pedersen, and Frede Blaabjerg. "A review of single-phase grid-connected inverters for photovoltaic modules." *Industry Applications, IEEE Transactions on* 41.5 (2005): 1292-1306.
- [35] Namboodiri, Anuja, and Harshal S. Wani. "Unipolar and Bipolar PWM Inverter." *International Journal for Scientific Research and Development* 1.7 (2015): 237-243.
- [36] OutBack Power." PV ground-Fault Detector Interrupter (GFDI) Installation Instructions.
- [37] Gubia, Eugenio, et al. "Ground currents in single-phase transformerless photovoltaic systems." *Progress in photovoltaics: research and applications* 15.7 (2007): 629-650.
- [38] Xiao, Huafeng, and Shaojun Xie. "Leakage current analytical model and application in single-phase transformerless photovoltaic grid-connected inverter." *Electromagnetic Compatibility, IEEE Transactions on* 52.4 (2010): 902-913.
- [39] Kerekes, Tamas, Remus Teodorescu, and Marco Liserre. "Common mode voltage in case of transformerless PV inverters connected to the grid." *Industrial Electronics, 2008. ISIE 2008. IEEE International Symposium on*. IEEE, 2008.
- [40] Di Piazza, M. C., F. Viola, and G. Vitale. "High Frequency Model of PV Systems for the Evaluation of Ground Currents."
- [41] Araneo, Rodolfo, et al. "EMC issues in high-power grid-connected photovoltaic plants." *Electromagnetic Compatibility, IEEE Transactions on* 51.3 (2009): 639-648.